OAK RIDGE
NATIONAL LABORATORY
MANAGED BY UT-BATTELLE
FOR THE DEPARTMENT OF ENERGY

ORNL/TM-2012/86

Annual Technical Progress Report of Radioisotope Power Systems Materials Production and Technology Program Tasks for October 1, 2010 Through September 30, 2011

March 2012

Prepared by
James F. King

UT-BATTELLE
ORNL-27 (4-00)

ORNL/TM-2012/86

Radioisotope Power Systems Materials Production and Technology Program
Materials Science and Technology Division

ANNUAL TECHNICAL PROGRESS REPORT OF RADIOISOTOPE POWER SYSTEMS MATERIALS PRODUCTION AND TECHNOLOGY PROGRAM TASKS FOR OCTOBER 1, 2010 THROUGH SEPTEMBER 30, 2011

J. F. King

March 2012

Prepared for
Department of Energy Office of Radioisotope Power Systems
AF 01 10 10 0

Prepared by
OAK RIDGE NATIONAL LABORATORY
Oak Ridge, Tennessee 37831-6079
managed by
UT-BATTELLE, LLC
for the
U.S. DEPARTMENT OF ENERGY
under contract DE-AC05-00OR22725

CONTENTS

Page

LIST OF FIGURES

Figure **Page**

Figure **Page**

LIST OF TABLES

ACRONYNMS

CBCF	Carbon Bonded Carbon Fiber
CCB	Configuration Control Board
CNC	Computer Numerical Control
CVS	Clad Vent Set
DAQ	Data Acquisition System
DOE	Department of Energy
DR	Deviation Request
EDM	Electrical Discharge Machine
EDS	Energy Dispersive Spectroscopy
FVA	Frit Vent Assembly
FY	Fiscal Year
GDMS	Glow Discharge Mass Spectroscopy
INL	Idaho National Laboratory
LANL	Los Alamos National Laboratory
LWRHU	Light Weight Radioisotope Heater Unit
MRF	Materials Research Furnace
NCR	Nonconformance Report
ORNL	Oak Ridge National Laboratory
PG	Pyrolytic Graphite
PWHT	Post Weld Heat Treatment
RPS	Radioisotope Power Systems
NASA	National Aeronautics and Space Administration
SEM	Scanning Electron Microscope
SIDR	Special Instruction Deviation Request
VAR	Vacuum Arc Remelted

ANNUAL TECHNICAL PROGRESS REPORT OF RADIOISOTOPE POWER SYSTEMS MATERIALS PRODUCTION AND TECHNOLOGY PROGRAM TASKS FOR OCTOBER 1, 2010 THROUGH SEPTEMBER 30, 2011*

J. F. King

1.0 INTRODUCTION*

The Office of Space and Defense Power Systems of the Department of Energy (DOE) provides Radioisotope Power Systems (RPS) for applications where conventional power systems are not feasible. For example, radioisotope thermoelectric generators were supplied by the DOE to the National Aeronautics and Space Administration (NASA) for deep space missions including the Cassini Mission launched in October of 1997 to study the planet Saturn. For the Cassini Mission, the Oak Ridge National Laboratory (ORNL) produced carbon-bonded carbon fiber (CBCF) insulator sets, iridium alloy blanks and foil, and clad vent sets (CVS) used in the generators. These components were also produced for the Pluto New Horizons and Mars Science Lab missions launched in January 2006 and November 2011respectively. The ORNL has been involved in developing materials and technology and producing components for the DOE for nearly four decades.

This report reflects program guidance from the Office of RPS for fiscal year (FY) 2011. Production activities for prime quality (prime) CBCF insulator sets, iridium alloy blanks and foil, and CVS are summarized in this report. Technology activities are also reported that were conducted to improve the manufacturing processes, characterize materials, or to develop information for new RPS. Work has also been initiated to establish fabrication capabilities for the Light Weight Radioisotope Heater Units.

*Research sponsored by the U.S. Department of Energy, Office of Space and Defense Power Systems, under contract with UT-Battelle, LLC.

2.0 PRODUCTION TASKS

2.1 CARBON BONDED CARBON FIBER

2.1.1 Background

The CBCF production facilities have been operated in a production maintenance mode since the Cassini campaign to produce prime insulators. Dedicated facilities for CBCF production remain in the Carbon Materials Technology Laboratory at ORNL. During much of the 1990s CBCF production was directed at making experimental variations of CBCF that explored the potential for improved insulating attributes at very high temperatures. The effect of brief excursions to reentry temperatures was also explored. Sleeves produced in FY 2000 were the first to be fully characterized in nearly a decade. Resolution of issues related to elevated impurities in CBCF allowed for continued production of prime insulators in FY 2003 through FY 2010. Prime insulator sets were shipped to Idaho National Laboratory (INL) in FY 2006 through FY 2008 to support the Mars Science Laboratory Mission. Production of prime insulators continued in FY 2010 and FY 2011 while implementing upgrades to production equipment and revision of numerous procedures.

2.1.2 CBCF Process Development

CBCF attributes and properties are defined principally by the selection of specific precursor materials and the intrinsic nature of the vacuum molding process. During the preliminary stages of CBCF development and refinement for the space power application, the selection of a specific fiber length for chopped rayon (~0.38 mm) and the use of a specific phenolic resin (Durez 22352) narrowed the range of possible outcomes for insulation made using the vacuum molding process. The ratio of resin to fiber in the slurry was selected to achieve adequate bonding and strength in the final insulators. The final char yield of the retained resin is approximately 20 weight percent and contributes to the final mass and density of insulators. Compressive strength and thermal conductivity correlate with density within the allowable range of the specification. Recent experience with shipping and handling of insulators for the Mars Science Laboratory mission suggests an advantage to producing insulators in the upper range of allowable density. This results in stronger, more chip resistant insulators that also meet the thermal conductivity specification.

Process development efforts in FY 2010 investigated the effect of slurry flow rates on the vacuum molding process. Slurry flow-rate programs were selected to achieve uniform densities in the final insulators while maintaining total vacuum molding times nominally equivalent with that used in previous production campaigns.

Vacuum molding of CBCF insulators employs a vacuum roughing pump and vacuum accumulator tank to sustain the flow of carbon fiber – resin slurry onto a flat filter-plate for disc preforms or cylindrical molds for sleeves billets. Vacuum molding is concluded with a one-minute vacuum dewatering step. Historically, only the initial vacuum level in

the accumulator tank was measured prior to molding. A process improvement effort was undertaken in FY 2011 that employed mechanical vacuum gages attached to key locations and electronic vacuum gages attached to sleeve mandrels. The vacuum dewatering stage in vacuum molding of CBCF plates and sleeve billets was identified having a significant effect on final density due to additional compaction of the wet preform that occurs. Vacuum levels were measured and recorded during molding and dewatering of numerous test runs. A vacuum regulator and vacuum relief valve were employed to adjust vacuum levels during dewatering. The vacuum measurements indicated opportunities to improve the vacuum molding and dewatering steps that should improve the integrity and consistency of the final insulators. Processes improvement steps were incorporated into prime production in FY 2011 under Special Instruction Deviation Requests (SIDRs). Process development runs performed during this effort are described here for CBCF discs and sleeves.

2.1.3 CBCF Plates for Discs

Five experimental plate runs TP-2011-1 through TP-2011-5 were carried out while measuring vacuum levels at several key locations in the vacuum molding system using bourdon tube gages. Measurement of vacuum level immediately below the filter-plate proved to be most indicative of the condition pertinent to molding. The pressure differential indicated by this gage during most of the vacuum molding operation was principally an indication of the pressure differential created by the hydrodynamic effects of the slurry flowing through the filter plate and into the vacuum accumulator. However, reading on this gauge was a quantitative measure of the pressure differential with respect to the ambient atmospheric condition. As all of the water was extracted from the slurry, the gage reading indicated the more conventional pressure differential associated with an empty volume.

All six test plates were carried out with the standard carbon fiber – phenolic resin slurry and at a constant flow rate of 4.5 gpm. The molding times were nominally 13 minutes for all runs. The first three runs, TP-2011-1 through TP-2011-3 were performed under the standard vacuum conditions including the dewatering step. Attempts to reduce vacuum levels in a couple of these runs using the vacuum regulator were unsuccessful because the high mass flow rate of the vacuum pump overwhelmed the pressure relief capability of the regulator. It was found that the vacuum level during dewatering could be reduced substantially by opening a large relief valve (V6) at the vacuum pump during the dewatering step. Three modified runs were made with V6 open, thereby effecting a 50% reduction in vacuum pressure differential during dewatering. Vacuum levels during vacuum molding two plate runs are plotted in Figure 1 for the two dewatering conditions described above. A substantial reduction in the peak and sustained pressure differentials during dewatering was achieved.

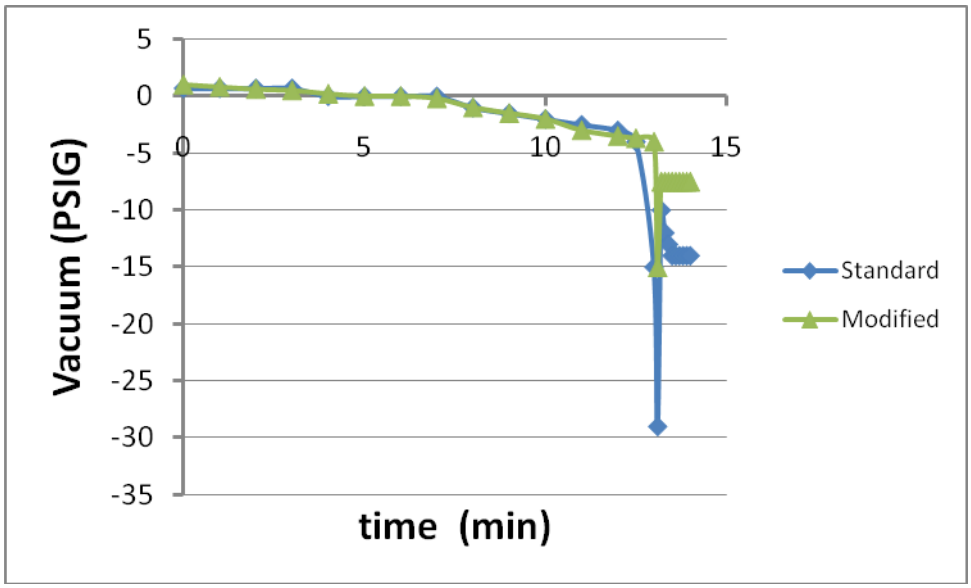

Figure 1. Vacuum pressure measured during vacuum molding and dewatering operations using both the standard configuration and modified configuration to reduce dewatering pressure by opening Valve 6 near the vacuum roughing pump.

2.1.4 CBCF Sleeve Billets

Three experimental sleeve runs TS 2011-1 through TS 2011-3 were carried out while measuring and recording the vacuum level inside six of nine sleeve mandrels using electronic vacuum sensors and a computer data acquisition system as illustrated in Figure 2. All test runs were carried out with the standard carbon fiber – phenolic resin slurry and at a programmed flow rate that varied linearly from 3 gpm to 6.75 gpm. The molding times were nominally 13 minutes to complete fiber deposition for all runs.

The vacuum readings measured inside six sleeve mandrels during a standard molding run are plotted in Figure 3. The offset in initial pressure differentials were not zeroed to allow for differentiation of the sensors in the plotted results. The pressure differential steadily decreases during vacuum molding as the vacuum slurry molding process deposits carbon fiber and resin on the sleeve molds. Following the standard procedure, when the main slurry tank is depleted and the level in the molding tank reaches the top of the sleeve molds, the center plug is removed to allow for rapid draining of slurry from the molding tank. The vacuum inside the mandrels is completely lost for about 30 seconds as indicated in Figure 3. The center plug is reinserted and vacuum dewatering begins under the draw from the roughing pump. The vacuum inside the mandrels abruptly returns to negative values. As the slurry deposition stage of vacuum molding is nearing completion, the flow of water from the slurry through the wet sleeve preform is replaced by the flow of air as a result of draw from the accumulator tank in the final seconds of molding and from the vacuum roughing pump during dewatering. The loss of vacuum with the center drain plug completely removed leaves the water-laden sleeve performs subject to slumping and shearing. This has historically resulted in frequently slumped and damaged sleeve billets.

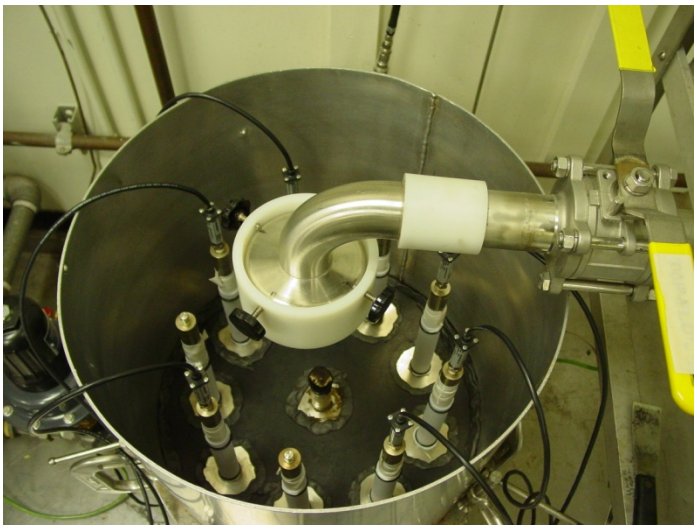

Figure 2. Sleeve molding tank showing six of nine sleeve mandrels fitted with vacuum sensors to measure pressure differentials during vacuum molding and dewatering. Note the plug at the center of the tank.

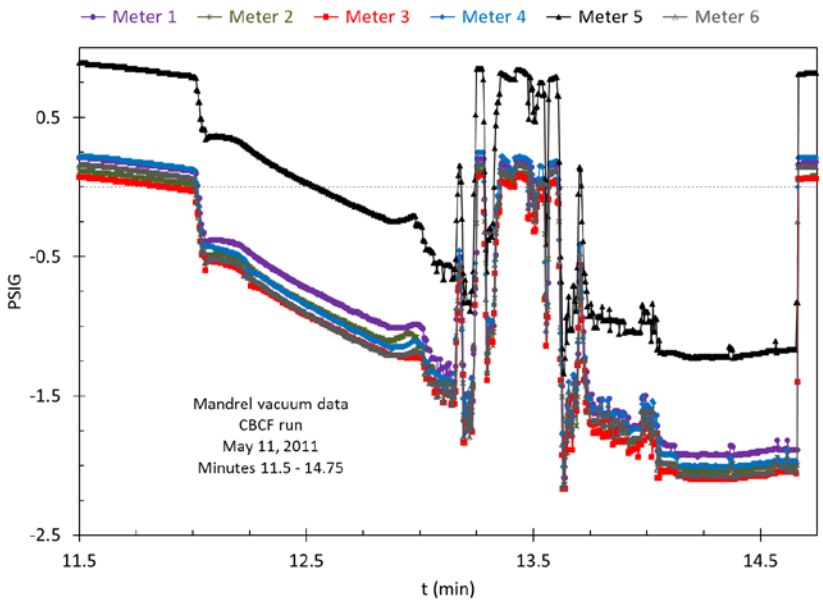

Figure 3. Vacuum measurements made inside six of nine sleeve mandrels during vacuum molding and dewatering operations using the pull-and-replace drain plug.

A rotary drain valve shown in Figure 4 was designed and installed to allow for draining of the molding tank without manual removal and replacement of the plug. The net result was maintenance of a vacuum within the sleeve billets during the draining operation as indicated by the vacuum readings in Figure 5. Several of the experimental runs were required to establish a suitable aperture size in the rotary valve. Sleeve runs E51 and E52 were made with the refined rotary valve to satisfy the FY 2011 production commitment. The vacuum molding procedure will be revised to include use of the rotary valve pending qualification of E51 and E52 Sleeves.

2.1.5 CBCF Production

Fifteen additional prime candidate CBCF insulator sets, comprised of E51 and E52 Sleeves and F22 Discs, were produced in FY 2011 to support future RPS Program missions. Qualification of these insulators will be completed in FY 2012. These three production runs were produced under SIDRs to allow the incorporation of process improvements described above. Numerous Quality Assurance Surveillances were conducted at ORNL including: instrument calibration, dimensional inspection of insulators, personnel training, and various production activities.

2.1.6 CBCF Qualification

Qualification tests were completed for CBCF insulators produced in FY 2010 including F21 Discs and E47 and E48 Sleeve lots. All qualification results were within the specification.

2.1.7 CBCF Production and Qualification Procedures

Two CBCF Production Procedures were revised including: MET-CER-SOP-29, "Preparation of Carbon Fibers" and MET-CER-SOP-32, "Drying Curing and Carbonization." Approval by the Configuration Control Board (CCB) will be sought in early FY 2012.

2.1.8 CBCF Production and Qualification Capability

Key personnel including the task manager, one principal technician and one machinist remain committed to the near-term (~5 years) production of CBCF insulators. A new technician was trained and qualified for radiographic inspection of CBCF insulators in FY 2011. Additionally, personnel involved in qualification testing will be available to support near-term production and training.

Facilities and equipment used for the production of CBCF are being upgraded. Additional vacuum gauges were used during vacuum molding operation to establish refined operating parameters for CBCF production as discussed in Section 2.1.2. Additional physical refinements to the vacuum molding system will continue in FY 2012.

Figure 4. Rotary drain plug allows for draining of slurry tank prior to dewatering without losing vacuum within sleeve mandrels.

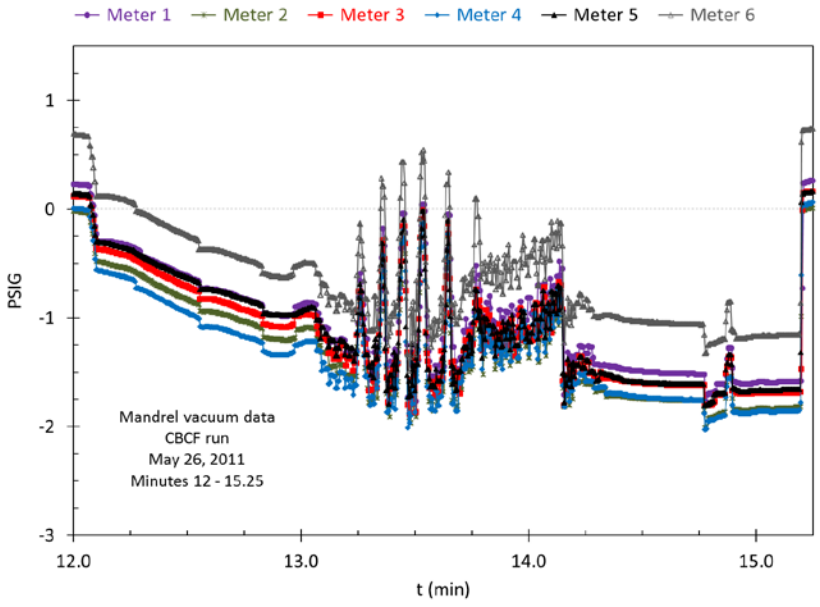

Figure 5. Vacuum measurements made inside six of nine sleeve mandrels during vacuum molding and dewatering operations using the rotary drain valve.

A new high-vacuum furnace was procured from Materials Research Furnaces (MRF) of Suncook, New Hampshire. This custom-built high vacuum furnace will employ a turbo molecular pump to achieve a vacuum of better than 10^{-7} torr at the 1500°C outgassing temperature. All utilities for the furnace were installed in FY 2011. Delivery to ORNL is planned for early calendar 2012. The contract with MRF includes commissioning of the system and training at ORNL.

2.2 IRIDIUM ALLOY BLANK AND FOIL PRODUCTION

The goals for this task are to produce prime blanks and foil under full configuration control, maintain production capability and to supply materials needed for CVS demonstration and maintenance activities. During FY 2011 a total of 14 blanks were produced. Blanks were stored with an approved data package.

2.2.1 Blank Production

Fourteen prime blanks were produced from the L1 ingot and the L-batch of powder was qualified for production use. Processing of 48 kg of iridium powder for the L-batch was begun in FY 2005. Eighteen kilograms of the powder was processed through blending, sintering, melting and extrusion in FY 2006 to produce the L1 extrusion. The extrusion had been stored for processing to blanks. During FY 2011, 14 prime blanks were produced from a portion of this extrusion.

The extrusion L1 was cut to produce 8 double-length rolling billets of approximately 10 cm length and single-length rolling billet of approximately 5 cm length. Traveler documents were issued for production of blanks from the single-length billet L1-1 and from two double-length billets L1-6, 7, and L1-14, 15. The three rolling billets were electrolytically cleaned in potassium cyanide in preparation for rolling. The three rolling billets were rolled to intermediate thickness. The double-length billets were cut in half to produce five sheets, identified as L1-1, -6, -7, -14, and -15. The sheets were cleaned in acid solutions, recrystallized, and hot rolled to final thickness. The sheets were then flattened using the Fenn rolling mill with large diameter steel rolls. The sheets were again cleaned in acid solutions and heated in vacuum at 900°C as a stress relief treatment.

Blanks were machined from three of the sheets, L1-1, L1-6, and L1-14, and the remaining two sheets were stored for future production. A total of 20 blanks were electrical discharge machined and surface ground along with 8 test pieces for destructive analysis. A total of 15 blanks passed the dimensional inspection. Two blanks did not meet the minimum thickness requirement, one blank did not meet the maximum diameter requirement, and two blanks did not clean up during grinding. The out of tolerance measurements were documented with a Nonconformance Report (NCR) (IrBF-2168) and the affected blanks were designated for use in tensile impact testing to qualify the L-batch of powder and also for weldability testing. The blanks and test pieces were cleaned and stress-relief heat treated in vacuum. Samples for chemical and metallographic analyses were prepared from the test pieces. All blanks passed the ultrasonic inspection. All but one blank passed the dye penetrant inspection. The blank was used for tensile impact testing purposes. All but one blank passed the visual inspection. This blank was

reworked by sanding using an approved procedure and it passed the subsequent required dimensional, dye penetrant and visual inspections.

Metallographic examination of a sample from each sheet showed that all materials met requirements for porosity, inclusion content, and microhardness. Samples from each of the three sheets were chemically analyzed and found to be within specified limits. One analysis for oxygen impurity content by the specified inert gas fusion method was deemed invalid when the high reported value was not consistent with "information only" oxygen results of the glow discharge mass spectroscopy (GDMS) for the same sheet. A repeat analysis by inert gas fusion of the material showed normal results.

The requirements for qualification of a powder batch for production use per the production procedures include metallographic and chemical analysis of material from locations near each end and the middle of the first extrusion produced from the powder batch. In addition, tensile impact testing of material from each of the three locations must demonstrate a minimum tensile elongation of 13.5% in tests at standard conditions of 980°C and 60 m/s. The results of these tests shown in Table 1 are sufficient to qualify the L-batch of powder for production usage.

Table 1. Results of Tensile Impact Testing of Duplicate Specimens from Three Blanks of the L1 Extrusion Under Standard Conditions of 980°C and 60 m/s

	Tensile Elongation, %	
Blank No.	**Spec. 1**	**Spec. 2**
L1-1-2	27.9	18.8
L1-7-7	21.4	30.8
L1-14-2	31.2	24.1

2.2.2 Powder of M-batch Powder

The M-batch of powder containing 82 kg of iridium was received, sampled, analyzed, and accepted in FY 2007. The powder was blended and prepared for further processing in FY 2010. In order to obtain additional assurance of the suitability of this powder for production use, a milestone was included in FY 2011 to process an initial quantity of this powder through electron beam melting and to analyze the impurity contents of the melted product. Since sampling and analysis at this step in the process is not routine, it was planned that the sampling and analysis of some five melted buttons from the batch blend M-1, containing 2865 grams, would be performed under an SIDR.

Powder blending and preparation of powder compacts was performed using the standard procedure. The subsequent sintering was performed in two furnace runs each at 1000 ±25°C for 60 ± 5 minutes. During the second furnace run containing compacts M-1-19 through -35, the programmable logic controller on the furnace terminated the hydrogen flow and switched to argon flow immediately following the completion of the 60-minute run. The compacts were moved to the cold zone, as normally performed. An attempt by the furnace operator to manually restart the hydrogen flow was not successful and the

compacts were cooled in argon gas rather than hydrogen gas. The likely cause of the hydrogen flow shut-off was a faulty intermittent signal from a flow or temperature sensor to the programmable logic controller causing the furnace to enter a safe shut down mode.

All of the compacts were then heated in vacuum at 1500°C for four hours and electron beam melted in accordance with the standard procedures to produce buttons numbered 1 through 5. Two buttons were sectioned for analysis, Button 2 consisting of compacts M-1-8 through -14 from the first furnace run and Button 5 consisting of compacts M-1-29 through -35 from the second furnace run.

The results of the analysis by GDMS of chemical impurities for the two buttons are listed in Table 2. Impurity elements not listed in this table, including carbon and oxygen analyzed by GDMS rather than the normal Leco methods, were below the detectability limit of 1 ppm or less. The impurity contents of Buttons 2 and 5 differ by less than 10% of the measured value or by 0.1 ppm, which is within the uncertainty limits of the analytical method. These results indicate that the cooling of the compacts in argon rather than hydrogen had no effect on the purity of the melted product.

Table 2. Impurity Content for EB-Melted Buttons from M-Batch Iridium Powder and Comparison to Averaged Historical Data for EB-Melted Buttons from L-Batch Iridium Powder and Sheets Produced From K-Batch Iridium Powder

Element	Impurity Content, ppm by Weight			
	M1-batch Button 2	M1-batch Button 5	L-batch EB-melted	K-batch Sheet
Si	3.4	3.4	1	1.8
Ti	0.4	0.4	0.34	1.3
V	0.15	0.13	0.03	0.03
Cr	0.04	0.01	0.01	
Mn	<0.01	<0.01	<0.01	0.03
Fe	0.14	0.03	0.03	
Cu	0.01	0.01	<0.05	0.2
Zr	0.3	0.3	0.2	0.15
Nb	0.45	0.45	0.08	0.14
Mo	1.7	1.6	1.3	1
Ru	20	19	26	8
Rh	0	1	1.1	2.1
Re	0.35	<0.35	<0.05	0.25
Pt	1.9	1.7	2.2	1.3

Table 2 also compares the impurity contents of the two buttons from M-batch material with the historical average impurity content of buttons produced from L-batch powder and the historical average impurity content of finished sheet material from K-batch powder. The impurity levels for the M-batch buttons are well below the specified maximum value of 25 ppm for Cr, 35 ppm for C, and 50 ppm for all others. The differences in the trace levels of impurities between the three batches following melting are associated with differences in the impurity contents of the original iridium powder batches received from vendors. Silicon, considered to be the most detrimental impurity element commonly found in iridium powder, is somewhat higher in the M-batch button than the average for K- or L-batch production materials. The average silicon content for the K, L, and M blended powder batches and of the respective materials after electron beam melting is shown in Table 3. Also shown is the impurity ratio for silicon, defined as the ratio of the impurity content following electron beam melting to that of the starting powder. Also shown is a theoretical impurity ratio as discussed in the technical publication, E. K. Ohriner, "Purification of Iridium by Electron Beam Melting", *Journal of Alloys and Compounds*, Vol. 461, No. 1-2, Aug 11, 2008, p 633-640. The observed variability in silicon impurity ratios is normal, as shown in the above reference. The slightly higher silicon content in the product is due to the higher silicon content of the received M-batch powder.

Table 3. Mean Silicon Impurity Contents for Both As-Received Powder Batches and Following Electron-Beam Melting

Batch	Powder	After EB Melting	Impurity Ratio
K	7	1.8	0.26
L	4.6	1.0	0.22
M	10	3.4	0.34
Theoretical			0.43

2.2.3 Equipment Major Maintenance and Purchases

2.2.3.1 Billet Preheat Furnace Installation

A new furnace for preheating of iridium alloy billets for extrusion was installed. Acceptance testing of the furnace, including heating at 1600°C for 3 hours, was also completed. The furnace is an alternative to the existing furnace purchased in 1994, which is now no longer reliable for use in iridium alloy billet heating. The new furnace was purchased with FY 2010 capital funds.

2.2.4 Training and Processing of Scrap Materials

Training of a second technician in the dye penetrant and visual inspection procedures was completed. A second metallographer was trained in the procedure for examination of blank, foil, and cups. Training was also conducted for a second technician in the operation of the extrusion press.

The RS17 iridium alloy scrap ingot was successfully hot extruded to sheet bar. The ingot was vacuum arc remelted (VAR) in 2009. It is planned to roll the extruded bar to sheet during FY 2012 to prepare blanks for training purposes in the CVS task and material for experimental uses. The material is expected to have chemistry that is close to the specification limits for blanks.

A total of 2.5 kg of iridium alloy scrap material was cleaned, button arc-melted and drop-cast to produce electrode segments for a planned RS-18 scrap electrode. The electrode will be VAR for training of personnel and for verification of the VAR melt process procedure.

A total of 10 blanks of iridium alloy scrap were cleaned and vacuum heat treated for use in the CVS task.

2.2.5 Material Characterization

2.2.5.1 Tensile Impact Testing

Tensile impact testing "for information only" was performed on specimens from ingots GR9, K2, and K3. The tests were performed at 980°C and 60 m/s (200 ft. /s) following heat treatment at 1500°C for 19 hours. The tensile impact test procedure provides an elongation of 13.5% or greater as an acceptable value for qualification of an iridium powder lot. The results of the tensile impact testing are shown in Table 4.

Table 4. Results of Tensile Impact Testing of Specimens from Ingots GR9, K2, and K3 under Standard Conditions of 980°C and 60 m/s

Ingot	% Elongation Specimen 1	% Elongation Specimen 2
GR9	20.2%	24.9%
K2	27.4%	
K3	16.5%	23.6%

2.2.5.2 Impurity Effects

One small ingot of DOP-26 alloy with controlled additions of 30 ppm Si was melted using tungsten di-silicide as the additive. The ingot was rolled and heat-treated. The analyzed silicon contents in duplicate tests were 31 and 32 ppm. The material was provided to the Iridium Alloy Characterization Task for evaluation.

2.2.6 Deviation Requests

The following class II DRs was approved in FY 2011:

DR-Ir-237 revised the MET-MatP-SOP-104, "Sampling and Cleaning Iridium DOP-26 Alloy Blanks". The sample sizes for carbon and oxygen analysis were changed to conform to those stated in the respective analytical procedures. Numerous minor operational and editorial changes were also made.

DR-Ir-238 revised the MET-MatP-SOP-101, "Rolling Iridium DOP-26 Alloy to Sheet for Blanks from Extruded Rolling Billets". A second furnace was added for preheating of rolling billets and calculation of roll pass reductions and mill gap settings is described in greater detail.

DR-Ir-239 revised the Procedure MET-NDT-Ir-U1, "Ultrasonic Inspection of Iridium Alloy Blanks". The procedure format was updated and the equipment and steps used in this inspection method are described in much greater detail.

2.2.7 Presentations

An invited presentation at **TMS 2011 Annual Meeting**, Feb 27-March 3, 2011, San Diego CA, by E. K. Ohriner, entitled "Processing Methods for Iridium and Iridium Alloys."

A presentation at **TMS 2011 Annual Meeting**, Feb 27-March 3, 2011, San Diego CA, by E. K. Ohriner, G. B. Ulrich, R. G. Miller, and W. Zhang, entitled "Surface Processing of an Iridium Alloy for Control of Emissivity."

A presentation at **International Conference on Tungsten, Refractory & Hardmaterials**, May 18 -21, 2011, San Francisco CA, by E. K. Ohriner and E. P. George entitled "Processing of High Purity Iridium Alloys and Effects of Impurity Elements."

2.2.8 Publications

E. K. Ohriner and E. P. George, "Processing of High Purity Iridium Alloys and Effects of Impurity Elements," in **Proceeding of the International Conference on Tungsten, Refractory & Hardmaterials VIII**, Metal Powder Industries Federation, Princeton NJ, 2011.

2.3 CLAD VENT SET

2.3.1 Maintenance Production Summary

Three CVS were produced in 2011 as part of the DOE CVS Production Maintenance program. CVS production facility operability was maintained throughout the year for 34 pieces of equipment. Training of personnel was maintained with 21 people for 74 CVS operations during FY 2011. Trend analyses were maintained for all part types. No adverse trends were noted at the end of the year. All six CVS surveillances, per the Surveillance and Process Monitoring Plan for the RPS Program CVS and CBCF Production Tasks, GPHS-QA-002, Revision G (Appendix B), were successfully completed during the year. The CVS surveillances are listed below.

Welding Equipment (Laser and Electron Beam)
Reinspection
Tooling Identification and Control
Measuring and Test Equipment
Instructions, Procedures, and Drawings
Personnel Training

2.3.2 Nonconformance Reports

Two nonconformance reports, NCR-CVS-077 and -078 were submitted and accepted in FY 2011. NCR-CVS-077 pertained to Procedure GPHS-XF-3624/25, Rev. S which required the use of a 10″ Monarch lathe during the trim and grind-to-length operations. A newly installed Sharpe lathe (Model 1118H) replaced the 10″ Monarch lathe. The procedure was not adequately reviewed prior to use to prevent use of the incorrect lathe. A SIDR should have been written to allow use of the new lathe. The seven affected cups were dispositioned for "use as is" and thus, maintained their prime status. The procedure was revised to revision 20 to incorporate use of the new lathe.

NCR-CVS-078 was for shield cup 3625-05-5386. The minimum height measured 15.023 mm versus the required minimum of 15.04 mm, while the vent notch depth measured 0.248 mm versus the maximum allowable depth of 0.20 mm. During the initial vent notch grinding operation the start and stop grinding wheel depths were not properly noted. This produced an excessively deep vent notch. After the prescribed rework for the deep vent notch (lapping) and grit blasting rework for grit blast deficiencies, the cup height was found to be shortened too much and the vent notch depth was not remedied. Note: the grit blast deficiency was remedied. The operator was re-instructed to note the start and stop grinding wheel locations to ensure the proper vent notch depth. The cup was dispositioned to be acceptable for prime use.

2.3.3 Deviation Requests

Nine deviation requests (DRs) were processed in FY 2011. This is part of an on-going effort to update procedures and tooling drawings. The nine DRs involved revising ten procedures and 34 tooling drawings. The DR numbers, procedure numbers with the new revision designations, and the procedure titles are listed below.

DR-CVS-089, GPHS-XF-3624/25, Rev. 20 – Vent/Shield Cup Fabrication
DR-CVS-090, GPHS-XF-3619, Rev. 14 – Decontamination Cover Fabrication
DR-CVS-091 (R1), GPHS-XF-3621, Rev. 13 – Frit Vent Backing Disc Fabrication
DR-CVS-092 (R1), GPHS-XF-3622, Rev. 13 – Frit Vent Cover Disc Fabrication
DR-CVS-095, GPHS-C-3621 and -3622, Revs. 11 – Frit Vent Backing Disc and Frit Vent Cover Disc Inspection
DR-CVS-096 (R1), GPHS-XF-3620, Rev. 11 – Weld Shield Fabrication
DR-CVS-097 (R1), GPHS-C-3620, Rev. 10 – Weld Shield Inspection
DR-CVS-100, GPHS-Y-006, Rev. 11 – Formed Iridium Cup Acid Stripping
DR-CVS-103, GPHS-XF-3620, Rev. 12 – Weld Shield Fabrication

Additional DRs are planned for FY 2012 to update the Mild Steel Cup Fabrication, Vent/Shield Cup Fabrication and Frit Vent Assembly procedures and the respective tooling drawings.

2.3.4 Microindentation Hardness Evaluations of Various Iridium Alloy Clad Vent Set Cup Conditions

In FY 2010 microindentation hardenesses were measured on destructive test specimens from cups in three conditions: (1) as-recrystallized (cup TC182), (2) sized + recrystallized (cup TC187), and (3) recrystallized + sized (cup TC177). The recrystallized + sized condition, which is the standard order of production processing, showed increased hardnesses mostly in the radius region, but also in the equatorial region compared to the polar region of the same cup as well as all regions of the other two cup/conditions. The hardnesses were comparable for all regions of the as-recrystallized and sized + recrystallized conditions. These results indicated that the sizing operation imparts cold work/strain primarily in the cup radius region and to a lesser extent in the equatorial region.

In FY 2011 two additional cups were evaluated. Cup TC184 was recrystallized, sized, and fully processed while cup TC183 was recrystallized, sized, accidentally dropped three to four feet during courtesy inspection for electrical discharge machining (EDM) of the vent hole, re-sized, and final processed. These results along with those from FY 2010, the historical production results, and the used witness specimen results are shown in Table 5. The data indicate that strain imparted after the recrystallization operation increases the microindentation hardness especially in the CVS cup radius and equator regions. The greatest increases are in the radius region. The highest overall hardnesses were found in the cup that had been dropped and re-sized. Presumably, this was the cup with the highest strain. The last line of data in Table 5 indicates that the 635°C/4 h air burn-off and 1250°C/1 h vacuum outgas operations serve as stress relief operations that relieve the imparted strains and lower the hardness of the bulk material.

Table 5. Microindentation Hardnesses for Iridium Alloy CVS Cups in Various Conditions

Condition and Blank/Cup Identity	Average Hardness (HV 1000 g_f) Pole	Radius	Equator
Recrystallize RS12-7-3/TC182	235	233	237
Size + recrystallize RS12-5-4/TC187	236	236	241
Recrystallize + size RS12-8-1/TC177	245	261	249
Recrystallize, size, drop, re-size, finish RS12-7-4/TC183	247	258	255
Recrystallize, size, finish – tested after grit blast RS12-7-5/TC184	241	254	250
Recrystallize, size, finish – tested after grit blast 9 production D-test cups	237	250	243
Recrystallize, size, finish – tested before grit blast 30 production D-test cups	240	250	245
Recrystallize, size, finish, air burn-off, vacuum outgas 4 Used witness specimens (3625-05-5104 and -5164)	225	233	223

Additional testing is planned for FY 2012. The mounted specimens from cups TC183 and TC184 will be removed from their mounts, heat treated (at 1250°C, 1375°C, or 1500°C), re-mounted, and tested. Based on these test results, two additional finished cups, TC180 (blank RS12-8-4) and TC185 (blank RS12-5-2), will be heat treated and tested.

2.3.5 Miscellaneous Maintenance Production

A new materials engineer reported to work in January, 2011 for the CVS and Light Weight Radioisotope Heater Unit (LWRHU) Manufacturing Tasks. He is being trained in all aspects of both tasks. Renovations of rooms 119 and 123 in building 2525 were started for improved CVS and LWRHU manufacturing capabilities. Numerous old pieces of equipment (lathes, grinders, EDM), cabinets, sink, excess piping, electrical conduit, wiring, switches, and disconnects were removed after the appropriate radioactive contamination, beryllium, and/or PCB surveys were completed. The Thompson Grinder, Micro-matic Precision Wafering Machine, Cincinnati Ingot Cutter and Cincinnati Cylindrical Grinder in room 123 were cleaned and painted along with a non-iridium 10″ Monarch lathe from room 119. The lathe and a cleaned non-iridium Bridgeport mill were moved from room 119 to 123 for tooling fabrication capability.

A new Sharp Industries, Inc. (Torrance, CA) 1118H high precision tool room lathe for the CVS trimming and grinding-to-length operations was installed in room 119 to replace the 10″ Monarch lathe that was defective and cost-prohibitive to repair because of its age. Blasocut 2000 Universal (Blaser Swisslube Inc. - Goshen, New York) coolant was added. The tool post grinders for CVS cup trimming and grinding-to-length were adapted to the new smaller lathe. Exhaust ductwork was fabricated and tested to certify the proper air flow. Initially, low air flow was measured due to a duct problem discovered near the exhaust fan. Sheet metal repairs were made and the proper air flow was achieved. The Fagor (Fagor Automation Corporation - Elk Grove, IL) model 20i-T digital readout was successfully calibrated. A dial indicator and a magnetic base were ordered, installed, calibrated for use as a secondary check of travel for the CVS cup trimming and grinding operations. Four machinists were trained successfully in the use of the lathe for CVS work.

A new Agie Charmilles model 20 die sinking EDM was purchased through EDM Systems (Cookeville, TN) and received for installation in room 119. It will be used to cut blanks and vent cup vent holes. It replaces a Cincinnati Vertical EDM built in 1968. The new EDM was purchased with FY 2011 capital funds.

2.3.6 Production Equipment Upgrades

High Temperature Vacuum Furnace A (with graphite hot zone for frit vent assembly sintering and diffusion bonding operations) modernization was completed in FY 2011 replacing the over-temperature controller, temperature controller, process logic controller (PLC), and recorder. Table 6 lists these changes.

Table 6. High Temperature Vacuum Furnace Equipment Upgrades

Equipment Purpose	New Equipment	Old Equipment
Over-Temperature Controller	Honeywell UDC 2500	Barber-Colman 560
Temperature Controller	Honeywell DCP 551	Honeywell DCP 700
PLC	Allen Bradley system	Divelbiss system
Recorder	Honeywell Minitrend QX digital recorder	Doric 245 paper recorder

Runs were made verifying that the new equipment operates equivalent to or better than the old equipment. Procedure GPHS-OP-001A was revised and approved incorporating the new equipment. Identical equipment was ordered and received for furnace B and will be installed in FY 2012.

2.4 IRIDIUM POWDER AND INVENTORY MANAGEMENT

The purpose of this work is to manage an iridium inventory for all heat source contractors with emphasis on the significant quantities of iridium located at the Los Alamos National Laboratory (LANL), INL, and ORNL to maintain a no-change iridium inventory through an annual write-off of inventory and processing losses.

2.4.1 Iridium Demand and Supply Schedule

The demand and supply schedule, prepared for contingent planning purposes, presents a strategy to assess the availability of iridium for all improving and producing activities by projecting future demands. An adequate inventory needs to be maintained to meet the needs of the NASA space exploration and defense missions. Table 7 indicates that enough iridium will be available for these missions.

The first part of Table 7 shows the estimated production demand factors for prime blanks and foil. The schedule of produced blanks and foil represents the quantity and timing for delivery or storage at ORNL. The ingots from new material represent the quantity produced from new iridium powder to make either blanks or foil. These ingots must be produced on a timely basis to meet the lead-time requirement to produce and deliver or store the blanks and foil.

The production of blanks and foil produces recyclable iridium material that can be placed back into the production process at ORNL. A greater economic benefit is realized by using recycled material, since the need to purchase powder from an outside vendor is reduced.

Refinable iridium scrap is also generated from the production of blanks and foil. This scrap is sent to a commercial refinery when a sufficient accumulation occurs at ORNL, funding is available for the refining, and it makes economic sense based on a comparison of refining costs to that of new material.

Process losses of iridium occur during the working of the material at ORNL, LANL, and INL. Losses also occur during the refining process. These inventory losses are written off annually.

The information contained within Table 7 can be summarized as follows. There will be an adequate supply of iridium powder to produce the hardware for NASA space exploration and defense missions and 98.1 kg will remain at the beginning of FY 2015.

Table 7. Demand and Supply Schedule Shows Factors and Provides Strategy to Ensure an Adequate Supply of Iridium Powder for NASA Space Explorations and Defense Missions

Factors and strategy	U. S. Government fiscal years			
	FY 2011	FY 2012	FY 2013	FY 2014
Production-demand factors				
Produced blanks[1]	14	10	10	10
Ingots from new material	0	0	0	1
Ingots from recyclable material	0	0	0	0
Produced foil (m^2)	0	0	0	0.5
Refining and process losses (kg)				
Refining gain (loss)	0	0	0	0
Processing gain (loss)	(0.6)	(1.5)	(1.5)	(3.0)
Supply strategy (kg)[2]				
Beginning balance of powder	122.0	118.1	117.1	116.1
Receipt of refined powder	0	0	0	0
Receipt of purchased powder	0	0	0	0

[1]Estimate of maximum number of blanks
[2]FY 2015 beginning balance of iridium powder is estimated to be 98.1 kg.

2.4.2 Annual Write-Off

The annual FY 2011 write-off of iridium inventory was completed in June. A total of 0.6 kg of iridium was written off as a normal operating loss. The write-off appropriately reduced the non-fund iridium inventory. This 0.6 kg loss was considered a normal operating loss compared to the history of iridium losses during the past several years.

2.4.3 Iridium Accountability Reviews

The review at ORNL was performed in May. The purpose of this review was to evaluate the accountability, physical inventory, and security of iridium at ORNL. It was concluded that the accountability, physical inventory, and security for the iridium was in place and operating in a proper manner. No recommendations were necessary.

The review at LANL was conducted in July. The purpose of this review was to evaluate the accountability, physical inventory, and security of the iridium at LANL. It was concluded that the physical inventory and security for the iridium was in place and operating in a proper manner. However, the accountability needs improvement.

Presently, an inventory report does not exist to account for the iridium inventory located inside PF-4. A recommendation was proposed to establish an inventory report to account for the iridium inventory inside PF-4.

2.5 WELDING

All production welding equipment was maintained in an operable state for the entire year. All welding procedures were updated to the recent ORNL RPS preferred format; minor changes were made to equipment operation and cleaning of tooling. Operators were trained on the changes to the procedures.

The surveillance on laser and electron beam welding equipment, tooling, and conformance to procedures was completed. A surveillance of laser and electron beam welding activities was performed throughout August 3rd to 10th, 2011. The full period covered by this surveillance is August 2010- 2011. Observations on nearly all electron beam and laser welds were performed during this review period. Operators were evaluated for the ability to operate the equipment, follow procedures, completion of paperwork, and maintaining parts, equipment and tooling in a clean state. A review of welding logbooks was conducted for the period of August 2010-2011 to determine the number of components welded, rewelded, and rejected. The surveillance was satisfactory showing that all production components welded for the review period were acceptable.

A review was performed to determine what high strain rate tensile test data exists for iridium alloy welds. The available data has been summarized and was presented at the quarterly meeting in Dayton, Ohio, on December 8, 2010. The review found that normal high strain rate testing performed at ORNL did not use four pole arc oscillation during welding of the test coupons, as is used in production welding. This may have created conservative data. The analysis of past research also showed that post weld heat treatment (PWHT) is beneficial in increasing the measured ductility during high strain rate tensile testing. The temperature and time required to improve the properties has not been studied sufficiently to provide recommendations to the program. Module reduction processing at INL may be providing unintended benefits of providing some level of PWHT, but is not quantitatively known. Limited tests of laser welds have shown higher test ductility than the current gas tungsten arc welds. Modification of test coupon dimensions may allow use of high strain rate tensile testing from welded clads, but the influence of reduced specimen size to the current database is not known.

The assessment of welding equipment needs for future additions, upgrades, and replacement has been completed. The assessment concluded that the RPS Program at ORNL deploys multiple welding processes for production of CVS components, welding and materials research and development and support of LANL heat source encapsulation production. These welding processes utilize equipment/systems that range from very modern to either not operational or in need of upgrades or replacement. Both the development and production electron beam welding systems depend on vacuum tube technology within the high voltage generation equipment. The current state of gas tungsten arc welding is severely limited as compared to past capabilities. A cost estimate was provided to upgrade and replace specific pieces of equipment.

2.5.1 Flow Testing

Long term testing of a mass flow meter was continued to develop an alternate method of measuring the flow rates of frit vent assemblies (FVAs). The flow meter was coupled to a computer data acquisition system (DAQ) to record data. Further evaluation of flow measurements showed that air contamination could bias mass flow measurements that extends the testing duration. A series of flow measurements were made on four FVAs with the approved bubble method and mass flow to compare methods. Additionally, both helium and nitrogen were used as testing gases to determine if an alternate gas may be used with the mass flow meter. These tests were repeated generally on a monthly basis. Gas flow through the frit appears to be in transitional flow with both molecular and viscous flow components occurring. Further work will be ongoing to further explain and predict the flow rate variance. Preliminary analysis of the data show good agreement between the methods. Nitrogen may have reduced variability over time.

2.5.2 LWRHU

A review of available laser marking systems was conducted and procurement of a 20 watt fiber laser marker was completed. Two craft support personnel and two engineers were trained in the maintenance and operation of the system. A standard operating procedure, required for Class IV laser systems, was created and approved.

Preliminary welding development was conducted using reject hardware from Mound Laboratory. Several methods of electron beam welding were evaluated for welding the vent cap assembly to the clad body. These methods involved different techniques for performing the circular weld and included table interpolation, beam deflection and the use of a rotary positioner. The use of a rotary positioner is the first priority, followed by beam deflection, are the preferred methods to perform this weld. Figure 6 shows an early development weld performed with a rotary positioner. Likewise, initial welding development was performed on the frit to vent cap weldment. Both laser and electron beam methods were performed on reject hardware. Laser welding (Figure 7) of the frit to vent cap weld is the preferred method to date. Additional weld development will be conducted in FY 2012 to meet program requirements using either ORNL produced hardware or Mound engineering use components.

Welding development tooling was designed, procured, inspected, and cleaned. It is ready for FY 2012 welding development use. Design work has progressed through two reviews with the manufacturer of the electron beam welding equipment to procure a rotary positioner that may weld up to ten components for each chamber pump down cycle. The positioner is being designed to accommodate a variety of components rather than solely for welding the vent cap assembly to the clad body. If funding is available, procurement of the rotary positioner will begin in FY 2012.

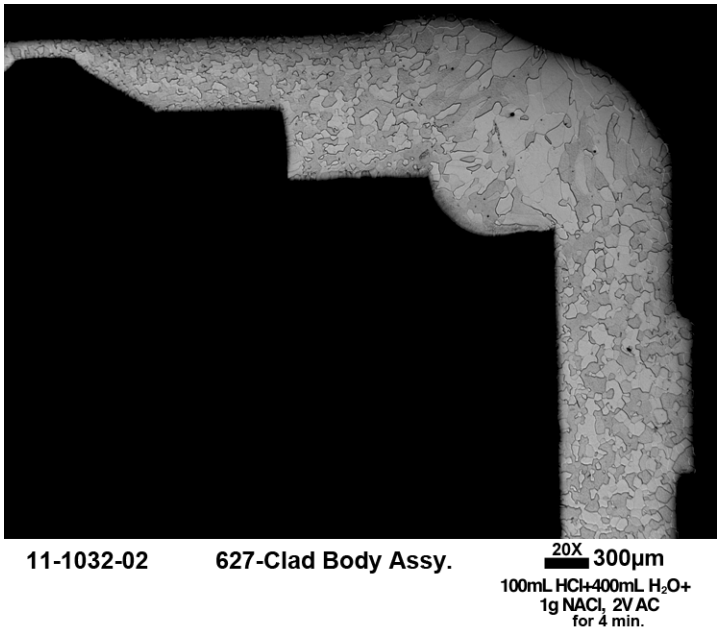

Figure 6. Preliminary Vent Cap Assembly to Clad Body Electron Beam Weld

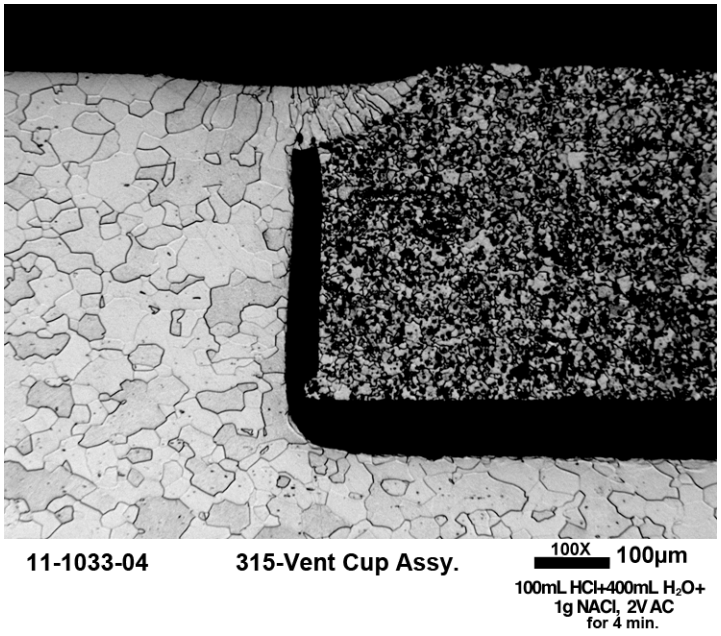

Figure 7. Preliminary Frit to Vent Cap Laser Weld

LWRHU precious metal components were transferred from INL to ORNL. A receiving inventory successfully verified the shipment inventory list. A database was created from the inventory list to track existing components and was also verified to be accurate.

All LWRHU component drawings were transferred to ORNL digital format. Engineering reviews were completed and these drawings are ready for final approval. Inspection gages used at Mound have also been transferred to ORNL digital format and are undergoing engineering review for accuracy. All applicable specifications and manufacturing procedures were converted to a draft document status. Modifications of the documents will be performed as needed.

A review of the Problem/Failure Reports (P/FRs) will be performed to gather lessons learned data in addition to Mound process flow charts and procedures in the planning of LWRHU component manufacturing. These documents are being requested from INL as they are identified. Additional documents were identified that potentially contain inspection or acceptance data on both machined components and raw materials. INL is searching for these and other documents previously requested.

2.6 LIGHT WEIGHT RADIOISOTOPE HEATER UNIT PRODUCTION STARTUP

An Epilog (Golden, CO) Fibermark 20 laser marking system was installed in room 119 and made operational. The standard operating procedure GPHS-OP-005 was completed and test samples were successfully marked. LWRHU Clad Body serial numbers will be laser marked using this system. The system will also be evaluated for potential use on the iridium alloy CVS cups.

Haas Automation, Inc. (Oxnard, CA) SL-10 and TL-1 lathes were installed for LWRHU Clad component machining. The SL-10 will be used for the majority of Clad Body machining while the TL-1 will be used for Clad Cap, Vent End and Closure End machining plus some Clad Body machining. Also a Sharp Industries, Inc. SG-618 manual surface grinder was installed for LWRHU Clad Cap, Closure End vent notching and possibly CVS cup vent notching.

LWHRU Clad Body machining was initiated using aluminum alloy 6061-T6 surrogate material. Ten aluminum Clad Bodies were machined as setup parts on the Haas SL-10 and TL-1 lathes. Dimensional inspection results indicated that small-radius tooling inserts will be required to consistently meet some of the Clad Body dimensional requirements. These inserts were ordered. Computer Numerical Control (CNC) programming will continue once they are received.

Frit cold pressing tooling, SKGBU9203, was designed, fabricated, and inspected. The tooling is ready for fabrication trials.

2.7 PYROLYTIC GRAPHITE COMPONENTS FOR THE LWRHU

The LWRHU is comprised of seven graphitic components that provide containment and thermal management for a single clad isotopic fuel pellet. The graphitic components for each containment include: one Fine Weave Pierced Fabric (FWPF) Aeroshell, two FWPF End Caps, one Pyrolytic Graphite (PG) Outer Insulator Body, one PG Middle Insulator Body, one PG Inner Insulator Body and two PG Insulator Caps. Existing material specifications and component drawings provide the basis for recapturing production capability and qualification of PG components for the LWRHU. Two domestic vendors were identified with specific expertise in the production of PG materials and machining of PG components. An attempt was made to execute a pre-qualification procurement of LWRHU PG components and specimens with both vendors to assess their capability to meet the current draft specification and satisfy quality assurance expectations. This effort will provide the basis for a formal vendor qualification plan. The task manager and program quality representative visited both PG vendors to provide a preliminary technical and quality assessment.

Vendor A is a technological leader in the production of PG components for a variety of commercial and government applications. This company produced LWRHU PG insulators for an earlier production campaign. The facility has maintained the physical production capability to make PG material and machine components. One machinist with specific experience making LWRHU components remains active. This vendor appears to have the facilities, quality assurance framework and personnel to produce acceptable LWRHU insulators. However, since they are lacking some formal government requirements to proceed with accepting the pre-qualification production procurement, they are lagging the second vendor in their current status on the program.

Vendor B routinely operates PG production furnaces comparable to Vendor A. Their extensive graphite and PG machining capability is managed by their companion company at the same location. A purchase order was placed with them for the production of three PG insulator sets and a series of test specimens. At the time of the technical-quality assessment, they had produced a preliminary set of insulators shown in Figure 8. Vendor B has the technical expertise to succeed in production of fully qualified insulators including one senior engineer who led LWRHU PG insulator production in a previous campaign. Vendor B initiated production of PG blanks late in FY 2011.

Figure 8. Preliminary PG insulator set produced by Vendor B.

3. BASE TECHNOLOGY TASKS

3.1 ALLOY CHARACTERIZATION

The iridium alloy that is currently used in radioisotope thermoelectric generators is referred to as DOP-26 and has the composition Ir-0.3W-0.006Th-0.005Al (wt. %). Over the years, researchers at the ORNL have studied the influence of impurities and alloying elements on the metallurgical and mechanical properties of iridium. Beneficial elements (e.g., Th [1], Ce [2, 3], and W [4]), deleterious elements (e.g., Si [5, 6]) and relatively benign elements (e.g., Fe, Ni, Cr, and Al [6]) have been identified as a result of those studies. Of the beneficial elements, two (Th and W) are added as alloying elements in DOP-26 iridium to provide the required properties (impact ductility and formability, respectively). The third beneficial element, Ce while not added to the currently used alloy, is available in the future as a partial replacement for Th if it becomes necessary to decrease the amount of radioactive Th in DOP-26 iridium. The presence of Si in excess of several hundred parts per million severely embrittles DOP-26 iridium under high-temperature impact conditions by segregating to the grain boundaries where it displaces beneficial thorium, promotes grain growth, and aids in the formation of a low-melting eutectic if present in sufficiently large concentrations. Therefore, its level in the alloy has to be kept low and studies are ongoing to determine a “safe” concentration below which it does not exhibit harmful effects on the metallurgical and mechanical properties of DOP-26 iridium.

This study continues our trace-element investigations and we report here the effects of tantalum additions (50 to 5000 weight part per million (wppm)) on the high-temperature tensile impact behavior of DOP-26 iridium. Tantalum was chosen for this investigation because, during CVS production, the DOP-26 iridium alloy is exposed to tantalum. Therefore, it is of interest to determine whether contamination with Ta can affect the mechanical properties of DOP-26 iridium. Here we report the effects of Ta concentration, heat treatment (i.e., grain size) and test temperature on the tensile impact ductility and fracture behavior of DOP-26 iridium.

3.1.1 Experimental Procedures

Tantalum was added at levels of 50, 100, 200, 500, 1000, 2500 and 5000 wppm to alloys having the nominal composition of DOP-26 iridium (i.e., Ir-0.3W-0.006Th-0.005Al, wt. %). The resulting alloys were arc melted, drop cast and rolled to sheet following the procedures used to make ‘old process’ DOP-26 iridium alloys. Dog bone-shaped tensile specimens with gage sections measuring $11.4 \times 2.5 \times 0.63$ (mm) were machined from the rolled sheets after they had been stress relieved for 1 h at 900°C. The surfaces of the specimen gage-sections were hand-polished with SiC paper through 600 grit; rinsed in acetone and ethyl alcohol, and given one of the following heat treatments in vacuum: 1375°C for 1 h, 1500°C for 1h, 1500°C for 19 h, or 1600°C for 1 h. Prior to impact testing, Vickers microhardness indents were made along the specimen gage lengths using a 500-g load and the distances between pairs of indents recorded.

High-strain-rate tensile tests were performed at temperatures in the range 800-1150°C using a gas-powered impact gun [1]. Before the specimens were inductively heated to the

test temperature, the test chamber was evacuated with a rotary mechanical pump and back-filled with argon gas. Specimen temperatures were controlled within ± 10°C and the specimens were allowed to equilibrate at the test temperature for 15-30 minutes before the test was started. The bullet velocity used for the impact test was 61 ± 3 m/s (which corresponds to an engineering strain rate in the specimen gage sections of ~5×10^3 s^{-1}). After each test was completed and the specimens allowed to cool, uniform tensile elongations were obtained by measuring the distance between pairs of microhardness indents, comparing them with the corresponding values before fracture, and averaging the results for each specimen. Fracture surfaces of select specimens were examined in a scanning electron microscope (SEM) to determine the fracture mode. Grain sizes were measured on small samples cut from the shoulder sections of impact tested specimens or from small specimens cut from the rolled sheets and annealed at different temperatures. The linear intercept method was used to calculate grain sizes and all measurements were made in the short transverse direction (i.e. on a plane normal to the rolling direction and in the through-thickness direction of the sheet).

3.1.2 Results and Discussions

Figure 9 shows the previously determined effects of 1-h anneals at the indicated temperatures on the grain sizes of old- and new-process DOP-26 iridium (containing no intentionally added Ta). For comparison, the grain sizes of some of the Ta-containing alloys were measured after a couple of different heat treatments to determine whether the addition of Ta significantly affected the grain growth behavior of DOP-26 iridium. We found that, after a 1-h anneal at 1375°C, the grain sizes of alloys containing 1000, 2500 and 5000 wppm Ta are not only similar to each other (17-23 µm) but also comparable to that of the Ta-free DOP-26 shown in Figure 9. The results of anneals at higher temperatures (up to 1600°C) and longer (2-h) showed similar trends, as listed in Table 8. Given these results for the higher Ta levels, we expect that the grain-growth behavior of the lower Ta alloys (50-500 wppm) will also be similar to that of the Ta-free DOP-26 alloy.

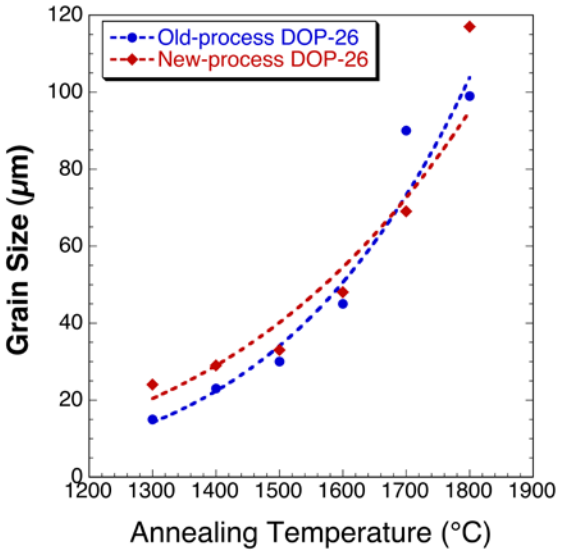

Figure 9. Comparison of the grain sizes of old- and new-process DOP-26 after 1-h anneals at the indicated temperatures.

Table 8. Comparison of the Grain Sizes (in µm) of Ta-Containing Alloys With Those of DOP-26 Iridium after Two Different Heat Treatments

	1550°C – 2h	1600°C – 2h
DOP-26 iridium	~50	~77
DOP-26 + 1000 wppm Ta	--	~75
DOP-26 + 2500 wppm Ta	~50	--
DOP-26 + 5000 wppm Ta	~53	~77

Figure 10 shows the temperature dependencies of the tensile impact ductilities of alloys containing 50 to 500 wppm Ta after 1-h anneals at 1500°C. For this heat treatment, the Ta-free DOP-26 alloy is expected to have a grain size of ~30 µm, as shown in Figure 9. Therefore, for comparison, the previously determined tensile impact ductilities of old-process DOP-26 iridium having comparable grain sizes (~27 and ~33 µm) are included in Figure 10. At temperatures below ~1000°C, the alloys containing up to 100 ppm Ta are as good as or better than the Ta-free alloy. At higher temperatures, all the Ta-containing alloys show somewhat lower ductilities than the Ta-free alloy, but additional tests are needed to determine the statistical significance of their lower ductility.

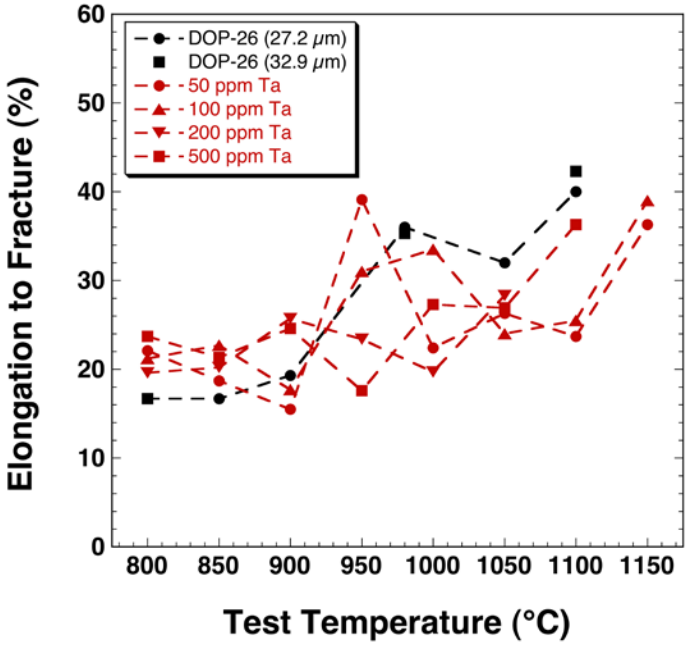

Figure 10. Temperature dependencies of the tensile impact ductilities of four Ta containing alloys after 1-h anneals at 1500°C. For comparison, the impact ductilities of DOP-26 iridium (containing no added Ta) are also plotted for grain sizes around 30 µm, which is the grain size expected in the Ta-containing alloys after annealing for 1 h at 1500°C.

Figure 11 shows the temperature dependencies of the tensile impact ductilities of alloys containing 50 to 500 wppm Ta after 1-h anneals at 1600°C. For this heat treatment, the Ta-free DOP-26 alloy is expected to have a grain size of ~45 µm, as shown in Figure 9. Therefore, for comparison, the previously determined tensile impact ductilities of old-

process DOP-26 iridium having a comparable grain sizes (~47 µm) are included in Figure 10. Over the entire range of impact test temperatures in Figure 11, the 50 and 100 wppm Ta alloys have ductilities that are comparable to or higher than that of the Ta-free DOP-26 alloy. While this is also true of the 200 and 500 wppm Ta alloys below ~1000°C, they appear to have somewhat lower ductilities at higher temperatures. To put these results in perspective, it is recalled that the minimum elongation required for qualification of iridium powder batches is 13.5% at 980°C after an anneal of 19 h at 1500°C. This heat treatment is used to simulate a possible accidental reentry scenario, during which the heat source is subjected to a short-term temperature spike of 3 minutes at 1900°C [1]. This anneal produces a grain size of ~50 µm, which is comparable to the grain sizes of the alloys shown in Figure 11. Since the 50 and 100 wppm Ta alloys have ductilities of ~20% or more over the entire temperature range tested, contamination with up to ~100 wppm Ta should not have any deleterious effects on the impact ductility of DOP-26 iridium.

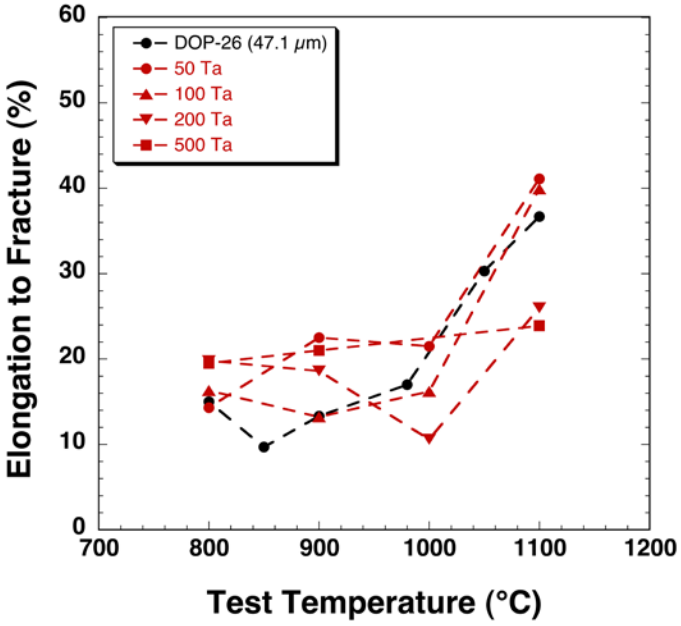

Figure 11. Temperature dependencies of the tensile impact ductilities of four Ta containing alloys after 1-h anneals at 1600°C. For comparison, the impact ductilities of DOP-26 iridium (containing no added Ta) are also plotted for a grain size of ~47 µm, which is the grain size expected in the Ta-containing alloys after annealing for 1 h at 1600°C.

The situation is dramatically different at higher Ta concentrations, as shown in Table 9, which lists the impact ductilities of the 1000, 2500, and 5000 wppm Ta alloys tested at 980°C after a 19-h anneal at 1500°C. As mentioned above, these are the same conditions as those used for qualification of iridium powder during DOP-26 blank production and, therefore, provide a useful baseline for comparison. The measured elongations were in the range of 4-6% and, within experimental scatter, did not exhibit a dependence on the Ta concentration. These ductilities are all significantly lower than the minimum elongation (13.5%) required for qualifying iridium powder during DOP-26 iridium production. They are also significantly lower than those obtained in tests on 21 different new-process ingots produced during the Cassini campaign (23 ± 5% elongation).

Table 9. Tensile Impact Ductilities of Ta-Containing DOP-26 Iridium (The alloys were tested at 980°C at a bullet velocity of 61 ± 3 m s^{-1} after annealing for 19 h at 1500°C.)

Specimen No.	0.1 wt.% Ta (% elongation)	0.25 wt.% Ta (% elongation)	0.5 wt.% Ta (% elongation)
1	3.8	4.1	4.6
2	4.5	5.2	6.4
3	3.6	3.9	8.0
4	4.4	4.0	5.3
Mean ± Std. dev.	4.1 ± 0.4	4.3 ± 0.6	6.1 ± 1.5

Generally, lower impact ductilities in DOP-26 iridium correlate with increased amounts of grain-boundary fracture [7]. To determine whether this was the case for the higher-Ta alloys, the fracture surfaces of the Ta-containing alloys were compared to those of DOP-26 iridium containing no added tantalum. As shown in Figure 12 (a-c), the fracture surfaces of the three Ta-containing alloys are similar but exhibit significantly more intergranular fracture than DOP-26 containing no added tantalum [Figure 12 (d)]. Clearly, the addition of Ta promotes brittle intergranular fracture in DOP-26 iridium.

Another possible reason for the observed intergranular brittleness is Ta segregation to the grain boundaries where it might promote decohesion. Generally, the driving force for an element to segregate to the grain boundaries varies inversely as its solubility in the bulk [9, 10]. In the case of Ta, however, as can be seen from the phase diagram shown in Figure 13, there is significant solid solubility (> 10 wt. %) of Ta in iridium. Therefore, one would not expect a large driving force for grain-boundary segregation.

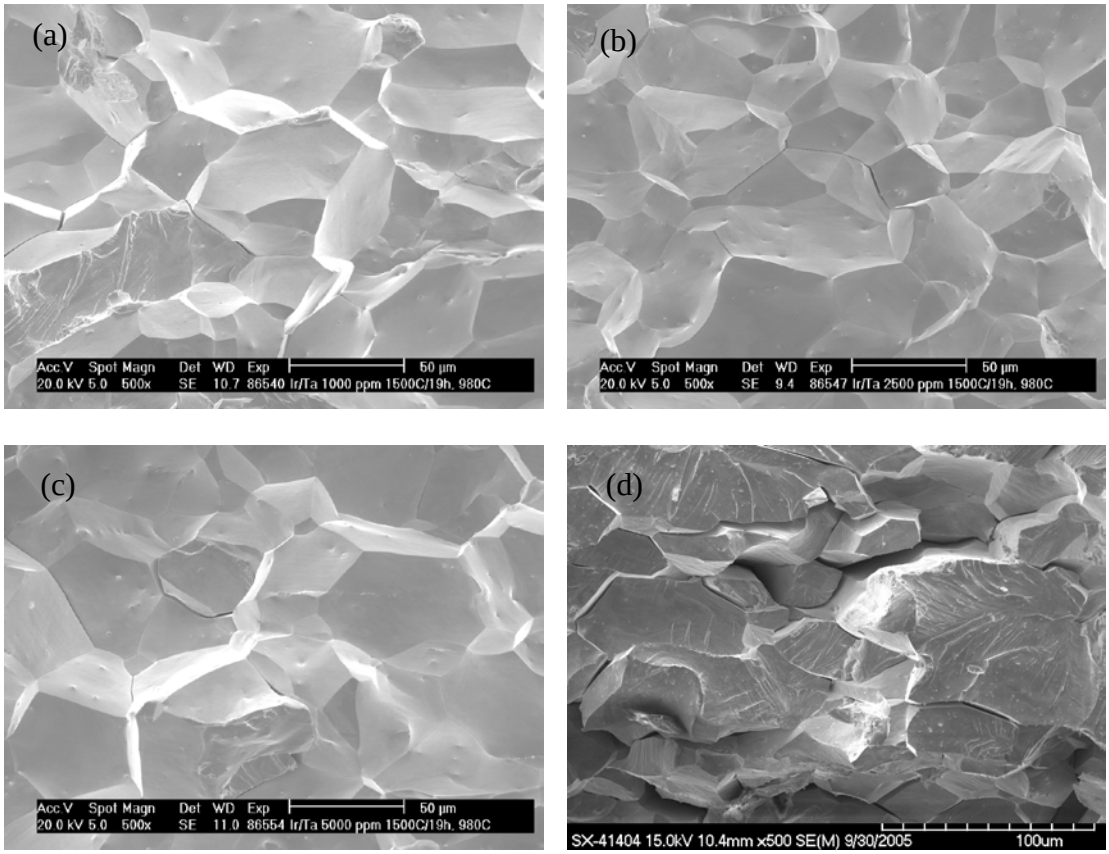

Figure 12. Fracture surfaces of the Ta-containing and Ta-free DOP-26 iridium alloys impact tested at 980ºC after annealing for 19 h at 1500°C: (*a*) 0.1 wt.% Ta; (*b*) 0.25 wt.% Ta; (*c*) 0.5 wt.% Ta; and (*d*) 0 wt.% Ta.

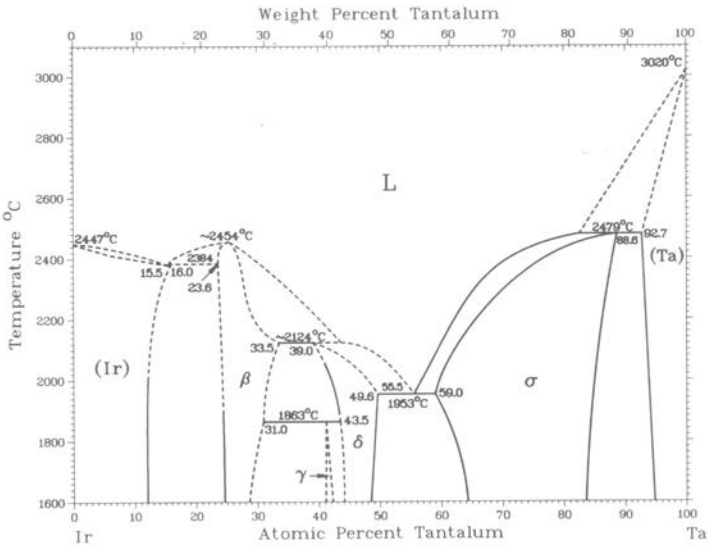

Figure 13. Ir-Ta phase diagram [11].

Figure 14 shows the temperature dependence of the tensile impact ductility of the 1000, 2500, and 5000 wppm Ta alloys after a 1-h anneal at 1375°C. For comparison, data obtained previously on DOP-26 iridium containing no added tantalum are also shown after the same heat treatment. The red inverted triangles represent the Ta-free alloy which is, in general, more ductile than the Ta-containing alloys. Within the experimental scatter, it is not possible to distinguish among the three Ta-containing alloys; however, as a group, they appear to be somewhat more brittle. However, this Ta-induced embrittlement is rather modest compared to the severe embrittlement noted in Table 8. The difference, of course, is that the grain size in the as-recrystallized state (~17-23 µm for all four alloys) is significantly smaller than after 19 h at 1500°C (~50 µm). As has been noted before [1], there are two principal factors that control the ductility and fracture behavior of iridium alloys: grain size and grain-boundary chemistry. It is possible that, for the results shown in Figure 11, grain size is the dominant factor, whereas for the results shown in Table 8, grain-boundary chemistry is the dominant factor.

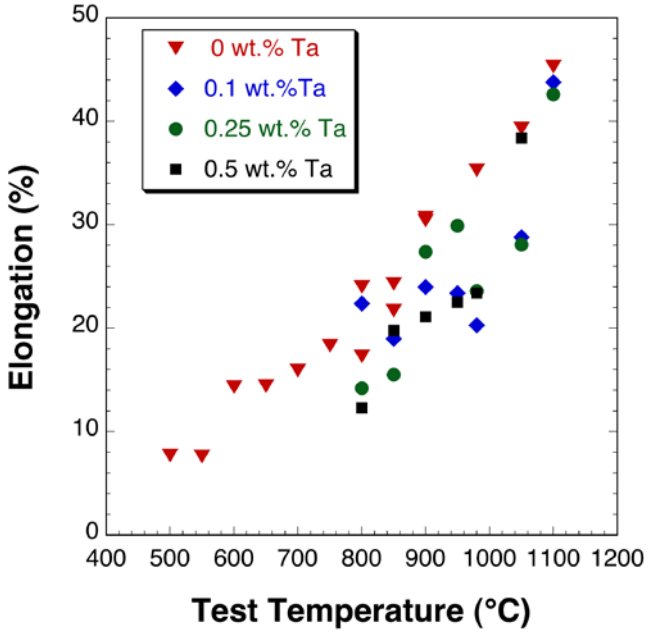

Figure 14. Effect of Ta on the temperature dependence of the tensile impact ductility of DOP-26 iridium. All alloys were annealed at 1375°C for 1 h, which is the standard recrystallization heat treatment given to the clad vent sets during production.

Figure 15 shows representative fracture surfaces of the three Ta-containing alloys after impact testing at 980°C in the as-recrystallized state. Consistent with their higher ductilities (Figure 11 versus Table 8), they exhibit considerably more transgranular fracture [Figures 15 (a-c) versus Figures 12 (a-c)].

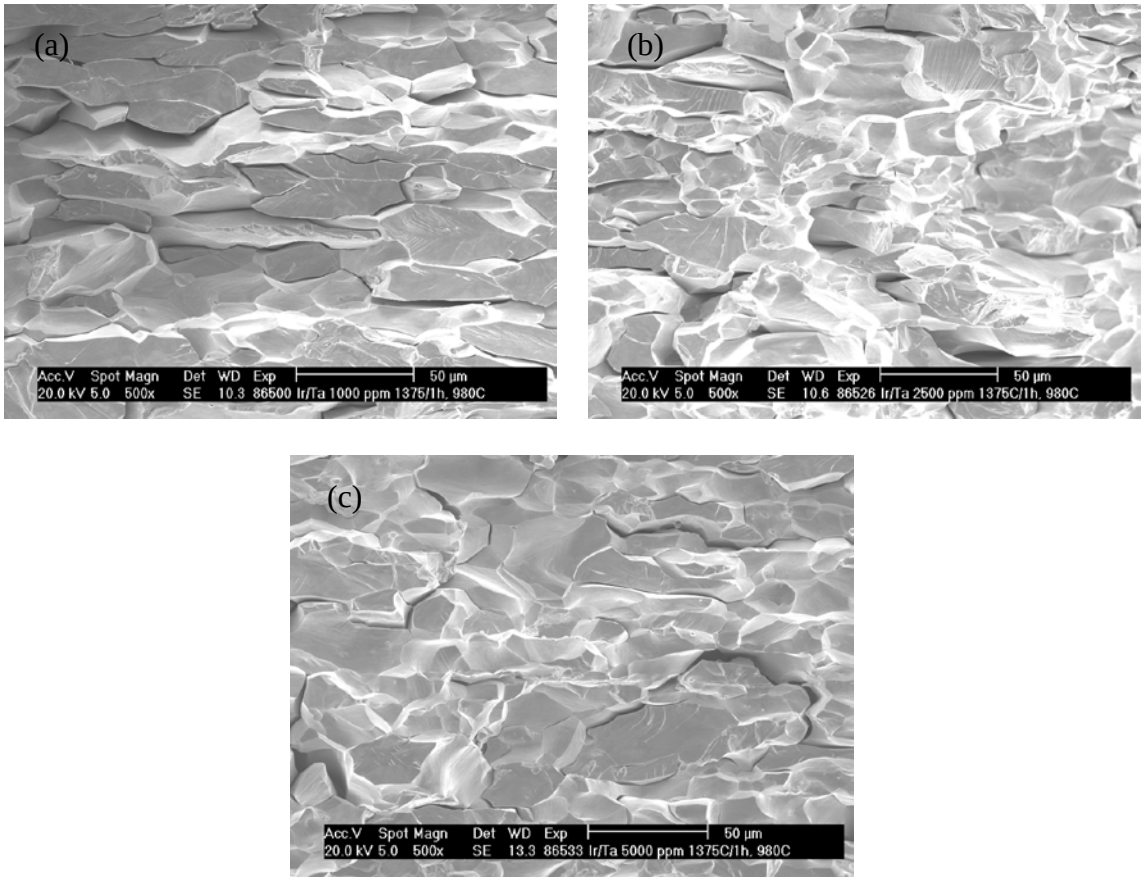

Figure 15. Fracture surfaces of Ta-containing DOP-26 iridium impact tested at 980ºC after annealing for 1 h at 1375°C: (*a*) 0.1 wt.% Ta; (*b*) 0.25 wt.% Ta; (*c*) 0.5 wt.% Ta.

3.1.3 Summary

Tantalum additions of 1000 to 5000 wppm severely embrittle DOP-26 iridium when its grain size is around 45-55 µm, but only modestly when its grain size is smaller, around 17-23 µm. Consistent with this, Ta promotes brittle intergranular fracture at the larger grain sizes but not at the smaller grain sizes. At levels below ~100 wppm, Ta does not embrittle DOP-26 iridium when tensile impact tested at temperatures up to ~1000°C after 1-h anneals at 1500 and 1600°C. The current specification limit of 50 wppm for Ta in DOP-26 is below the level where Ta has been found in the present study to be harmful for impact ductility.

3.1.4 References

1. C. T. Liu, H. Inouye and A. C. Schaffhauser, *Effect of Thorium Additions on Metallurgical and Mechanical Properties of Ir - 0.3 pct. W Alloys*, Metall. Trans. **12A** 993-1002 (1981).

2. A. N. Gubbi, E. P. George, E. K. Ohriner, and R. H. Zee, *Influence of Cerium Additions on High-Temperature Impact Ductility and Fracture Behavior of Iridium Alloys*, Metall. Mater. Trans. **28A**, 2049 (1997).

3. E. P. George, C. G. McKamey, E. K. Ohriner, and E. H. Lee, *Deformation and Fracture of Iridium: Microalloying Effects*, Mater. Sci. Eng. A, **319-321** 466-470 (2001).

4. E. P. George and C. T. Liu, *Micro- and Macro-Alloying of Ir-Base Alloys*, in Iridium (eds. E. K. Ohriner, R. D. Lanam, P. Panfilov and H. Harada), pp. 3-14, The Minerals, Metals and Materials Society, Warrendale, PA (2000).

5. L. Heatherly and E. P. George, *Grain-Boundary Segregation of Impurities in Iridium and Effects on Mechanical Properties*, Acta Mater. **49** (2) 289-298 (2001).

6. C. G. McKamey, E. P. George, E. H. Lee, E. K. Ohriner, and J. W. Cohron, *Impurity Effects on High-Temperature Tensile Ductility of Iridium Alloys at High Strain Rate*, Scripta Mater. **42** (1) 9-15 (2000).

7. C. G. McKamey, A. N. Gubbi, Y. Lin, J. W. Cohron, E. H. Lee, and E. P. George, *Grain Growth Behavior and High-Temperature High-Strain-Rate Tensile Ductility of Iridium Alloy DOP-26*, ORNL-6935, Oak Ridge National Laboratory, Oak Ridge, TN, April 1998.

8. C. G. McKamey, E. P. George, E. H. Lee, J. L. Wright, and E. K. Ohriner, *Grain Growth Behavior, Ductility, and Weldability of Cerium-Doped Iridium Alloys*, ORNL/TM-2002/114, Oak Ridge National Laboratory, Oak Ridge, TN, June 2002.

9. M. P. Seah and E. D. Hondros, *Grain-Boundary Segregation*, Proc. Roy. Soc. A **335** 191-212 (1973).

10. E. D. Hondros and M. P. Seah, *Grain-Boundary Activity Measurements by Auger-Electron Spectroscopy*, Scripta Metall. **6**, 1007 (1972).

11. *Binary Alloy Phase Diagram*s (Editor-in-Chief: T. B. Massalski) American Society for Metals, Metals Park, OH (1986).

3.2 MICROTHERM INSULATION TESTING

ORNL conducted testing to evaluate the behavior of Microtherm insulation when subjected to a variety of service conditions. Microtherm is a high temperature fibrous insulation material used in the generator housing.

Samples were subjected to elevated temperatures under vacuum and argon environments and both isothermal and gradient temperature conditions to evaluate four areas of concern as identified below.

a. Delamination Problems
b. Thermal Shock
c. Long-Term Degradation of Properties under Gradient Temperatures
d. Heat Dump Conditions.

Testing under the four identified conditions is further described below. The results of testing were expected to aid in the design and prediction of long-term behavior of the Microtherm over the life of a prospective mission.

Microtherm material was obtained in the form of a 160 x 160 x 50.8 mm block. Rectangular samples (25.4 x 25.4 x 50.8 mm) were periodically cut from this block for testing as shown in Figure 16. The cutting procedure consisted of securing the Microtherm block using a 152 mm (6″) vacuum plate with a 117 kPa (17 psi) vacuum. The samples were cut using a 3 mm (0.125″) diameter by 76 mm (3″) long helical end mill with a 25 mm (1″) cutting length. With each cutting pass, ≈16.5 mm (0.65″) of material was removed from the sample. Additionally, a vacuum cleaner was used during cutting to keep the cutter from loading up.

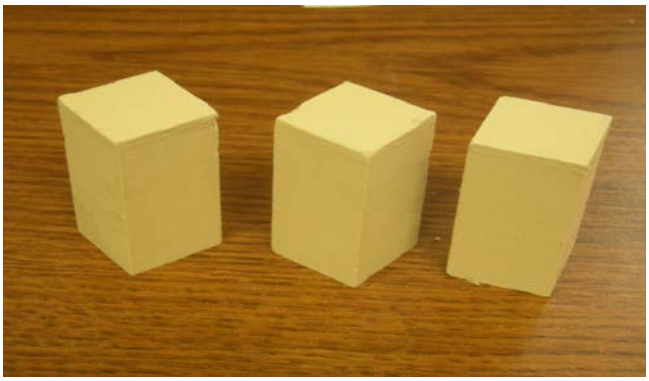

Figure 16. Rectangular (25.4 x 25.4 x 50.8 mm) Microtherm test samples.

3.2.1 Evaluation of Microtherm Delamination Issues

Delamination of Microtherm was previously noted when material was isothermally heated to temperatures of 650 and 950°C[1]. It was proposed to perform in-situ testing of Microtherm materials to observe shrinkage (dimensional changes) with temperature exposures over time. A transparent furnace system produced by Thermcraft Incorporated of Winston Salem, North Carolina[2] (shown in Figure 17) was use for this testing.

Figure 17. Trans Temp transparent furnace produced by Thermcraft used for evaluation of Microtherm delamination issues.

Unlike conventional furnaces, a gold mirror is used in these furnaces for insulation which provides transparency and allows for rapid heat up and cools down times with a uniform temperature zone over most of the length of the furnace. A quartz tube is then utilized to house the sample and to allow the equipment to operate under vacuum or inert atmosphere through the incorporation of vacuum or gas fittings on the ends of the tube. A resistive coil element is used to provide heating to a furnace chamber area that measures 57.15 mm (2.25″) ID x 304.8 mm (12″) long as shown in Figure 18.

[1] R. Elisii, "EU Microtherm Insulation Cracks witnessed after Dynamic Testing", Lockheed Martin Report PIR-U-ASRG-0068, (6/21/09).

[2] (http://www.thermcraftinc.com/transtemp-furnaces.html)

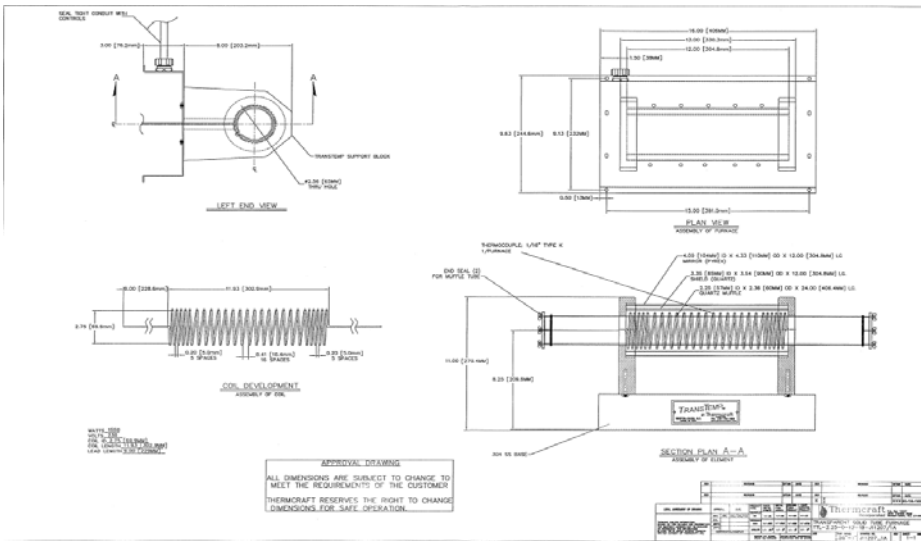

Figure 18. Schematics for Trans Temp transparent furnace showing heating element and dimensions.

A high-resolution video camera (Allied Vision Technologies Pike with a NAVITAR TV 7000 Zoom lens) was used to provide sufficient resolution for monitoring the dimensional changes of the Microtherm during testing. Testing consisted of monitoring the Microtherm sample as it was isothermally heated from room temperature to elevated temperature and then held. Several tests were run. Results from one test are discussed below as a characteristic example of this testing. A series of sample images from various temperatures and times during the heating of this test are shown in Figure 19 with the outline of the sample highlighted at each temperature. When the outlines of the samples at the various temperatures during heating are overlaid (as shown in Figure 20), no change in the sample size is observed from 22 to 400°C. Then, from 400 to 600°C, growth (as opposed to expected shrinkage) is seen. The sample remains at a constant size from 600 to 850°C.

Following heating, the sample was allowed to remain at temperature (850°C) for 190 hours. Again, a series of sample images (this time from various times at constant temperature) were collected as shown in Figure 21, with the outline of the sample again highlighted. When the outlines of the samples at the various times during the isothermal hold are over laid (as shown in Figure 22), there is a slight decrease in sample size observed with a time. This is the anticipated observation.

It should be noted that one of the original primarily goals of this task was to determine the cause of delamination previously observed in bake out testing performed prior to this test effort. Delamination was not observed in the samples described above; therefore no conclusions were possible regarding the delamination mechanism(s).

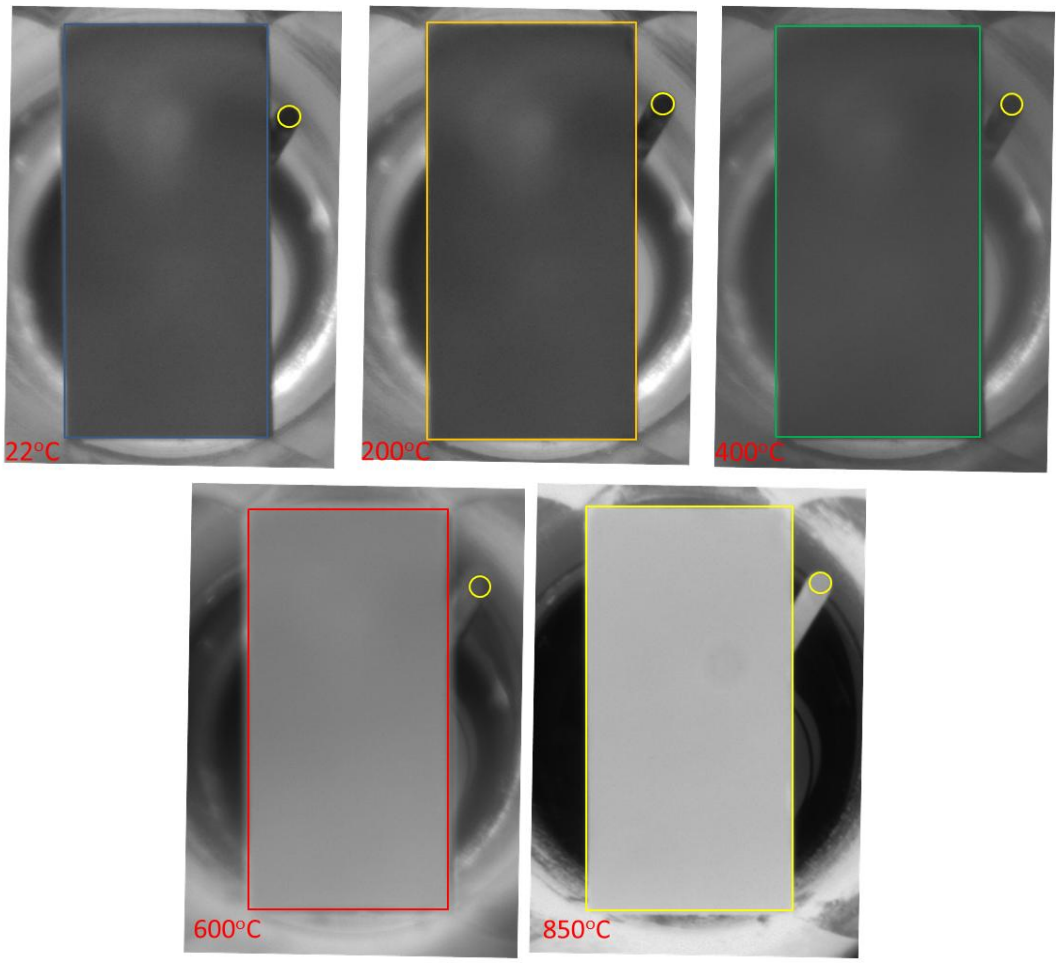

Figure 19. High-resolution images taken at various temperatures during heating of third transparent furnace test.

(RT-850°C at a rate of ≈4.5°C/min., yellow circle is thermocouple for reference)

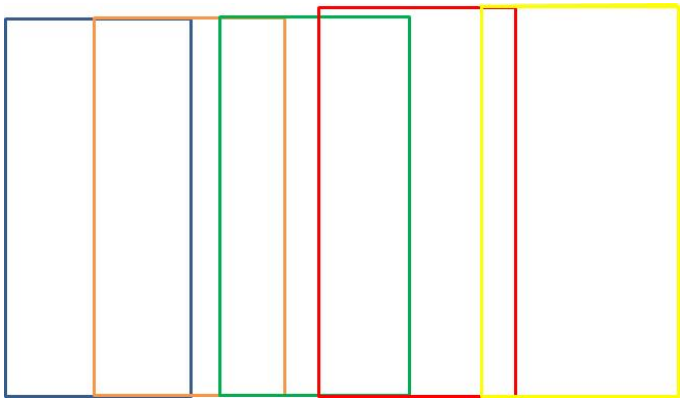

Figure 20. Over lay of sample outlines from high-resolution images taken at various temperatures during heating of second transparent furnace test as shown in (blue = 22°C, orange = 200°C, green = 400°C, red = 600°C, yellow = 850°C)

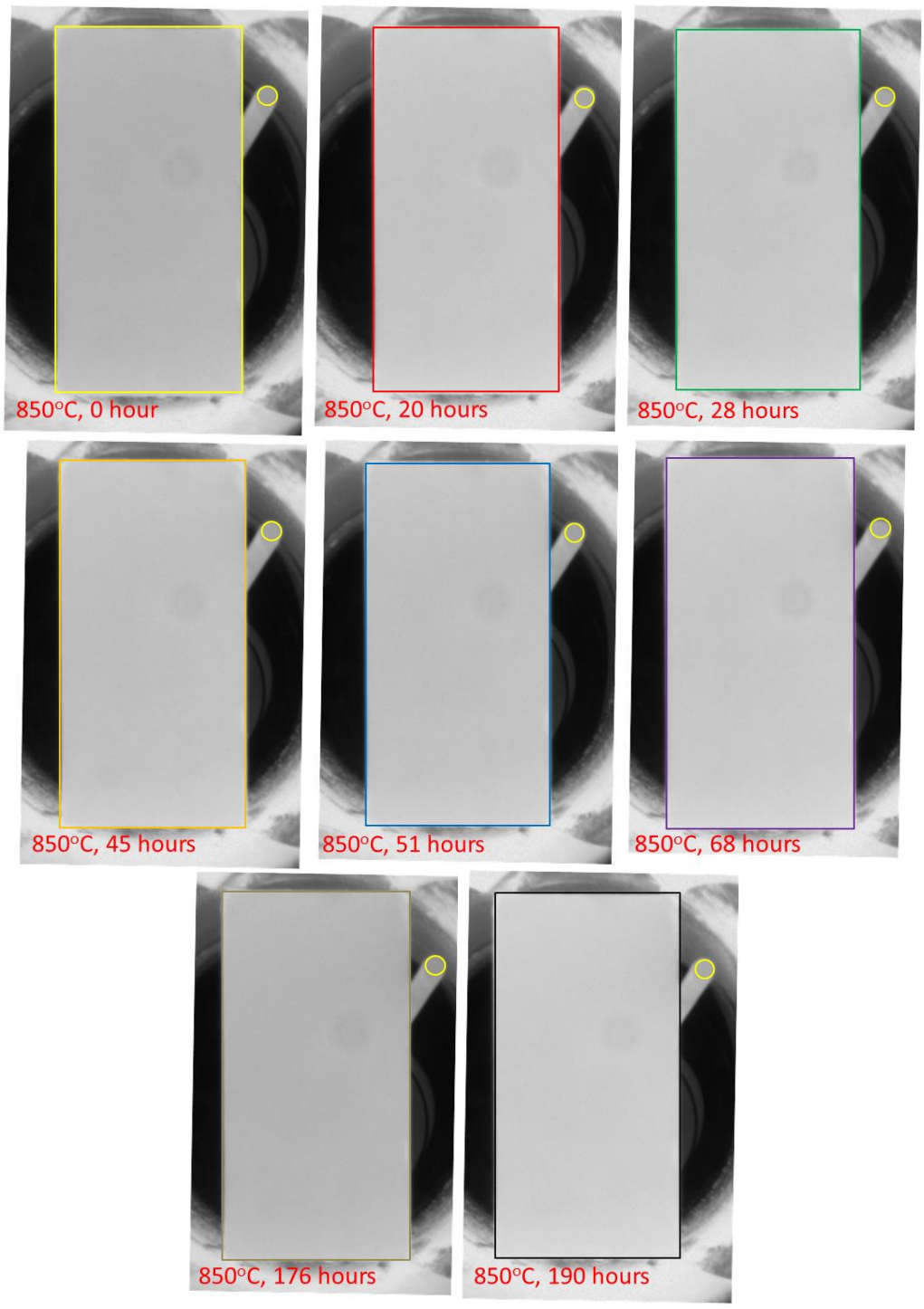

Figure 21. High-resolution images taken at various times during hold of third transparent furnace test. (hold at 850°C for 190 hours, yellow circle is thermocouple for reference)

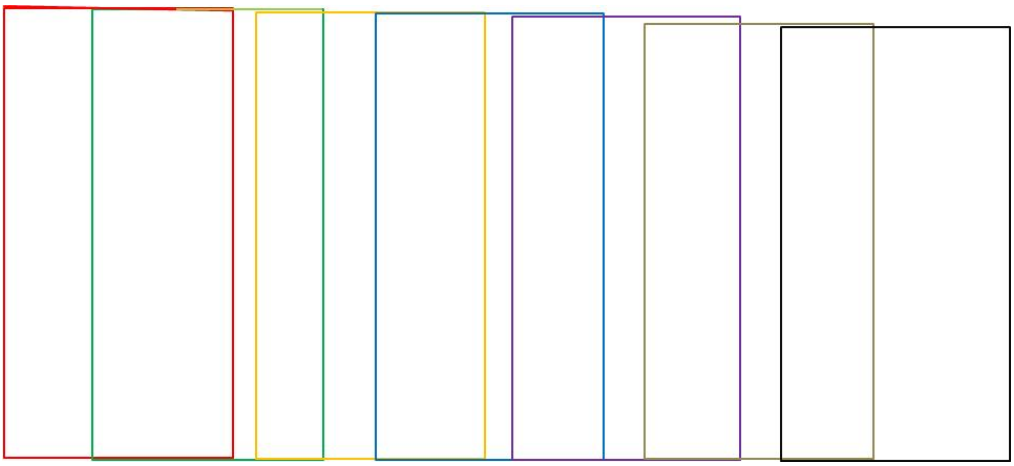

Figure 22. Over lay of sample outlines from high-resolution images taken at various times during hold of third transparent furnace test as shown in Figure 19. (yellow = 0 hour, red = 20 hours, green = 28 hours, orange = 48 hours, blue = 51 hours, purple = 68 hours, brown = 176 hours, black = 190 hours)

3.2.2 Thermal Shock of Microtherm Due to Introduction of Fueled Heater

Rapid heating was applied to Microtherm samples to simulate what is expected when the heater is lowered into the insulated housing at fueling. Testing involved the rapid heating of Microtherm within a vacuum chamber (shown in Figure 23) through the use of induction heating (Lepel T-30-3-KC-TL, 68 KVA, 460V, 85A) to closely simulate the actual temperature conditions experienced by the lining material during introduction of the fueled heater. Following heating, samples were analyzed visually and through microstructural evaluation of both pre- and post-baked samples to identify and analyze the mechanism(s) of the delamination phenomenon being observed in Microtherm and to possibly infer corrective actions that may be taken to correct this based on an understanding of the mechanism(s). Optical microscopy and Scanning Electron Microscopy (SEM) were utilized to provide an understanding and insight into the shrinkage and delamination that are seen in the material due to elevated temperature exposure.

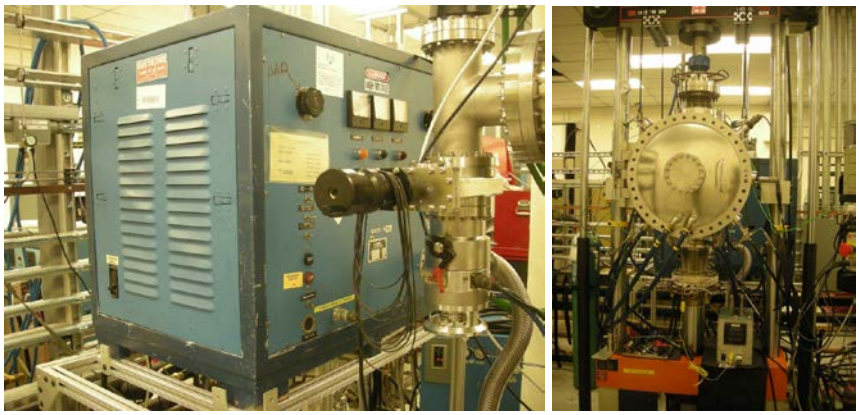

Figure 23. Lepel vacuum induction furnace used to simulate thermal shock of Microtherm due to introduction of fueled heater and the evaluation of Microtherm under "Heat Dump" conditions.

Refractory samples were encased in a steel sleeve surrounded by an alumina cylinder. The steel sleeve acts as the susceptor within the copper induction coil to supply heat to the Microtherm sample. A thermocouple was embedded between the susceptor and the sample to record the Microtherm temperature during heating.

Initial tests were run using Min-K insulation material from a previous project to tune the induction heating system, confirm temperatures measured, and determine heating rates. Only one Microtherm sample (25.4 x 25.4 x 50.8 mm) was tested under this Task using the heating schedule shown in Table 10.

Table 10. Heating Schedule Used for Thermal Shock Testing

Lepel Power Setting (%)	Temperature Target (°C)	Heating Rate (°C/min.)
10-18	700	5
18	700	(30 minute hold)
50-75	930	≈135

A picture of the sample before and after testing is shown in Figure 24. A cracking or delamination of the sample was seen approximately ¼ of the way from the top of the specimen after heating.

a)

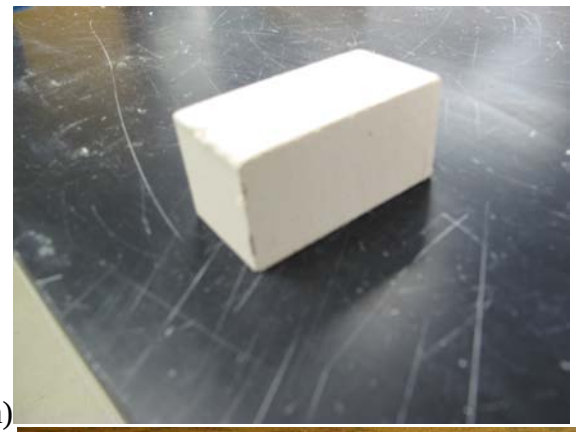

b)

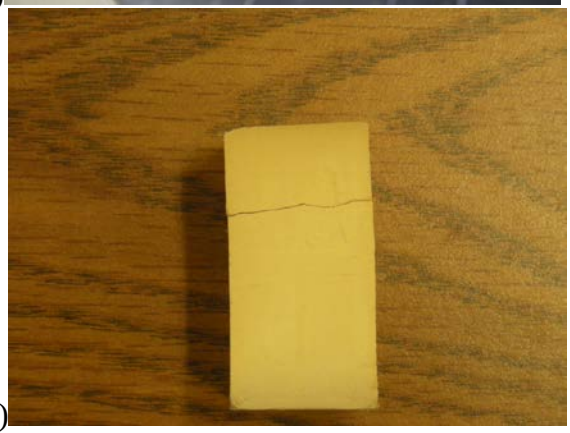

Figure 24. Comparison of Microtherm sample before (a) and after (b) thermal shock testing.

3.2.3 Long-Term Degradation of Microtherm Properties under Gradient Temperature Conditions

Testing was performed under a simulated gradient temperature environment under vacuum or argon, similar to actual conditions Microtherm insulation will be subjected to in service. Previous experience at ORNL regarding elevated temperature testing of insulation materials under gradient temperature conditions was drawn upon to design and implement such testing for Microtherm. The resulting data was then used to predict long-term behavior using models previously developed to predict behavior (out to 50,000 hours or more) based on limited experimental data (ranging from 1,000 to 17,500 hours).

The test apparatus was built for performing the gradient testing consisted of a three zone furnace (ATS 3210, 3300W, 230V, 4.8 A/zone) with digital Honeywell controllers, an alumina vacuum tube, and molybdenum TZM alloy push rods. Vacuum fittings and sensors (Linear Variable Differential Transformer (LVDT) system for measuring sample dimensional changes via an Invar rod and type K thermocouples) were prepared for this frame, along with metallic platens (Rene 141) to facilitate the needed gradient testing conditions as shown in Figure 25. The top platen was heated by the top zone of the three zone furnace attached to this frame, while the bottom platen was actively cooled by a portable chiller connected to cooling coils in contact with the platen. The incorporated thermocouples monitored the top and bottom platen temperatures. Data collection (temperatures and LVDT signal) was performed using in-house prepared LabView software.

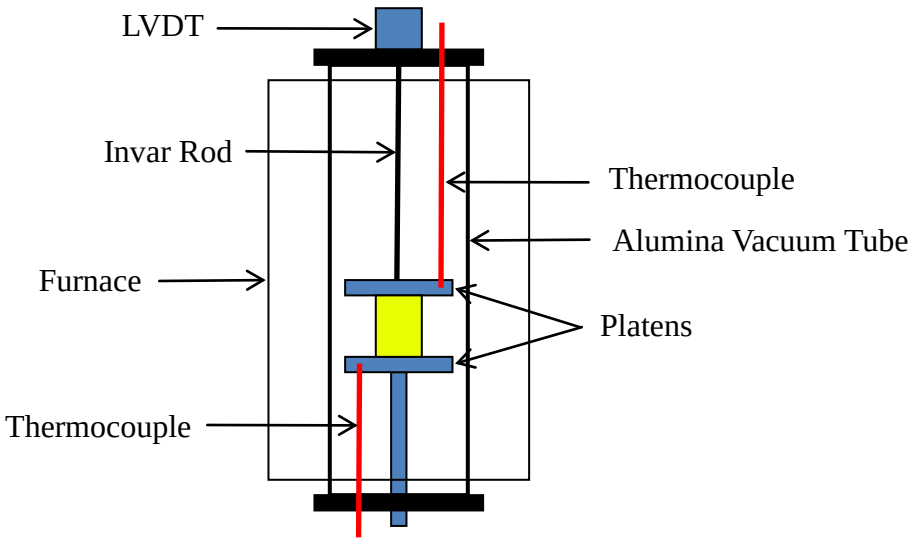

Figure 25. Modified test system for gradient testing.

While Microtherm samples were being prepared, initial testing to evaluate temperature gradients possible with this set up was performed using Min-K insulation (Thermal Ceramics, Augusta, GA) material from a previous project. Testing was also performed using a stainless steel sample of known thermal expansion. This allowed for the removal of the thermal expansion due to the load train from subsequently generated heating data.

Initially, six gradient tests were performed with an upper platen temperature of 850°C and a lower platen temperature of 250°C. Three tests (A, B and D) were performed under a vacuum environment and three tests (C, E and F) were performed under an argon environment. The Microtherm shrinkage for each of these six tests is shown in Figure 26. Additionally, a log equation ($y = a*\ln(x) + b$) was used to fit each shrinkage curve for each test. These log curve fits, along with an estimate of fit (R^2), are also shown in Figure 26. An average curve was then generated for the vacuum environment and the argon environment test conditions based on the three curve fits generated for each environment. These average curves are shown in Figure 27.

SEM/EDS analysis was performed on Microtherm samples following gradient testing. As seen in Figure 28, substantial cracking and fiber pull-out were observed by SEM in tested samples. The composition of the tested Microtherm material following gradient testing was found by EDS to consist of aluminum, silicon, titanium, and oxygen. Carbon was also seen due to the coating used to prevent charging of the SEM sample. Samples prior to testing were found to consist primarily of silicon and oxygen with some titanium present.

Isothermal testing of Microtherm samples at various temperatures was also performed in an effort to generate shrinkage data that could be used to form a mathematical model to predict shrinkage over any gradient temperature condition of interest. This effort was based on previous work conducted at ORNL regarding modeling and prediction of gradient stress relaxation behavior of Min-K thermal insulation material. Testing was conducted at 200, 400, 600, 700, and 800^{o}C for various durations with testing generally carried out until shrinkage leveled off (except for the 800^{o}C test, which was carried out for 250 hours). A summary of testing is shown in Figure 29 along with the same log equation ($y = a*\ln(x) + b$) fit and estimate of fit (R^2) used previously to model gradient shrinkage estimated for each isothermal curve.

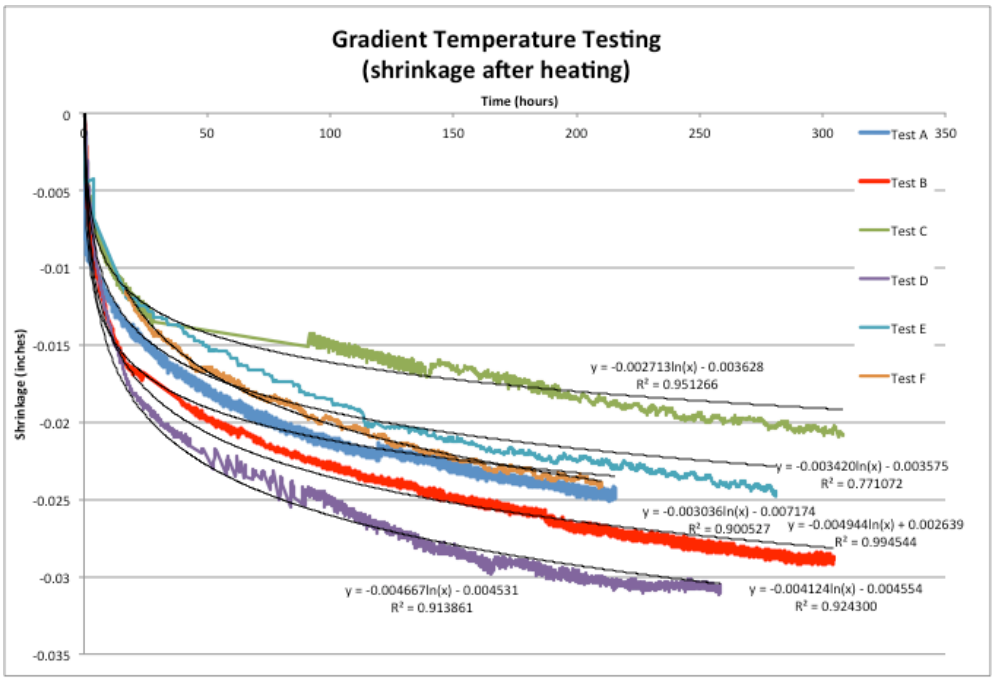

Figure 26. Summary of gradient test data (850-250°C) with log fit curves. (Tests A, B and D performed under vacuum, Tests C, E and F performed under argon)

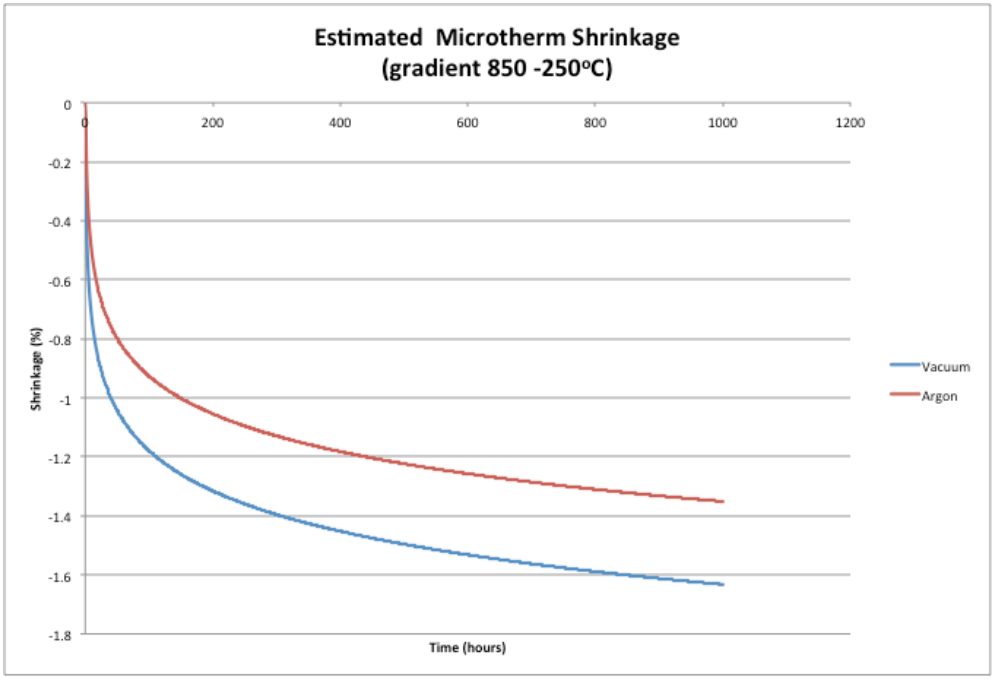

Figure 27. Average curves for vacuum and argon environment gradient test conditions (850-250°C) based on log fit curves shown in Figure 26.

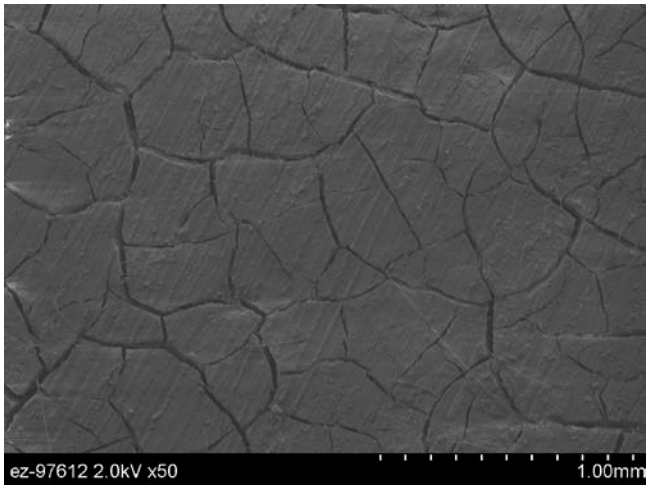

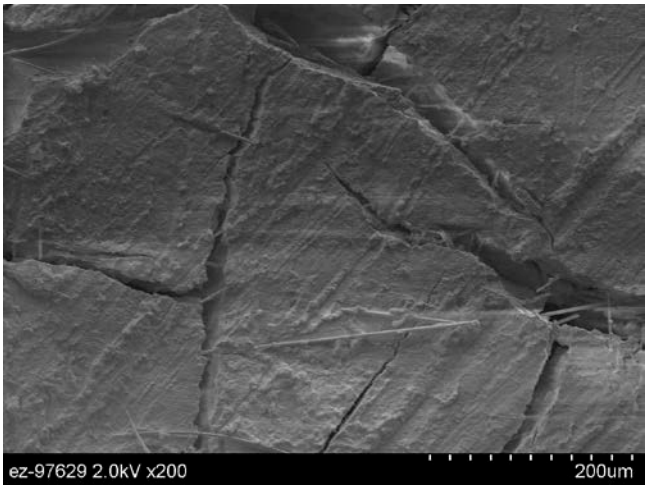

Figure 28. SEM micrographs of Microtherm following gradient testing.

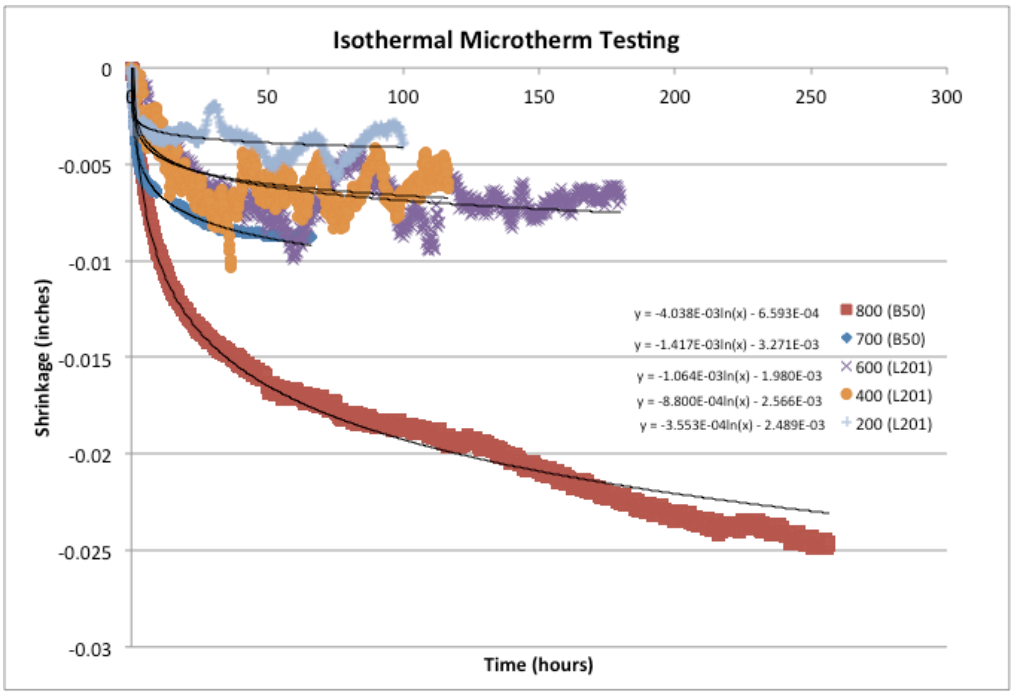

Figure 29. Summary of Isothermal test data with log fit curves.

The log curve fits for each temperature where then used to form a comprehensive model to estimate Microtherm shrinkage over any temperature gradient. This was done by first dividing a 50.8 mm high sample into twenty equal sections and assuming that the temperature gradient of interest was equally divided among these sections. The coefficients (a and b) from the log fits at each temperature were then plotted and fitted to a second order polynomial for each data set. This yielded equations, which were then substituted into the original log equation and used to calculate the Microtherm shrinkage versus time at various locations through the thickness of the 50.8 mm high sample (0, 12.7, 25.4, 38.1, and 50.8 mm) as shown in Figure 30 for a temperature gradient of 850-250^{o}C. It was found that the total predicted Microtherm shrinkage fit well with the actual average measured shrinkage from Figure 25 using the governing equation (1).

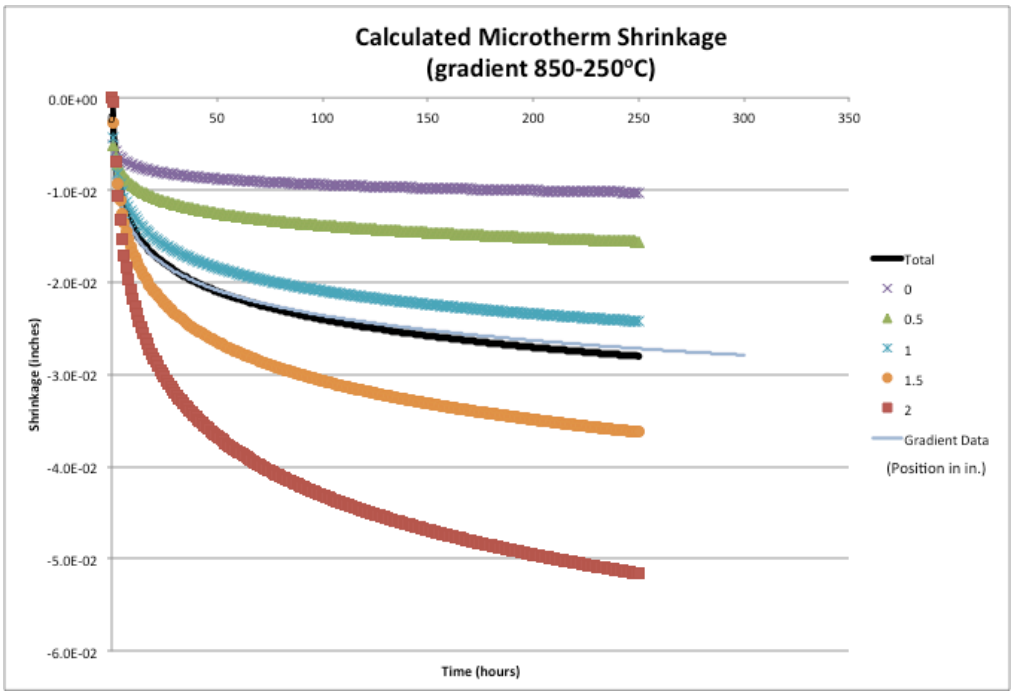

Figure 30. Predicted Microtherm shrinkage at various locations within a 2" specimen based on gradient temperature at that location (colored lines), total predicted shrinkage (black line) and data from actual gradient testing (thin blue line) from Figure 25.

$$y = a*\ln(t)-b \quad (1)$$

where: $a = -8.786E\text{-}9*x^2 + 2.648E\text{-}6*x - 5.335E\text{-}4$

t = time in hours

$b = -8.738E\text{-}9*x^2 + 5.700E\text{-}6*x - 1.695E\text{-}3$

x = temperature in °C of sample location

Based on the success of this prediction, a follow-on gradient test was run under a vacuum environment with a temperature gradient of 600-200°C. A similar analysis was then run using the log curve fit model developed above and the new temperature gradient of 600-200°C. A comparison of experimental and predicted gradient data collected over this temperature range is shown in Figure 31 along with the previously reported data for the temperature range of 850-250°C as shown in Figure 30. Again, it was found that the total predicted Microtherm shrinkage over the 600-200°C gradient fit well with the actual average measured shrinkage from experimental testing. An additional long-term gradient test was started after completion of this work. This test was still on-going at the end of the FY 2011.

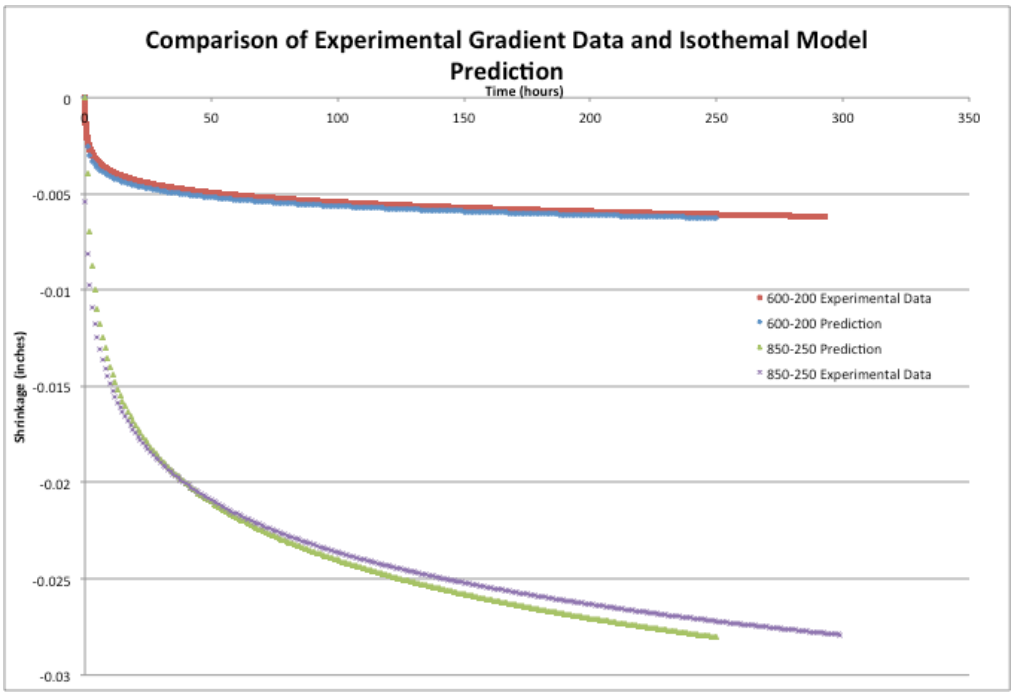

Figure 31. Comparison of predicted and actual experimental Microtherm shrinkage for two temperature ranges of interest.

3.2.4 Evaluation of Microtherm under "Heat Dump" Conditions

Rapid heating of Microtherm insulation was performed utilizing the same set-up developed for the Thermal Shock testing (see Figure 23**)** to simulate an event where the engine fails and the module heats up rapidly in what has been termed a "heat dump" condition. Under such conditions, there is concern that the Microtherm insulation within the module may overheat and shrink resulting in an increase in thermal conductivity which could then lead to cooling of the fuel clads. This testing evaluated the effect of such heating on the Microtherm dimensional stability and microstructure was evaluated.

Microtherm samples (25.4 x 25.4 x 50.8 mm) were prepared for testing using the heating schedule shown in Table 11. This schedule was designed based on heating data provide by Lockheed[3] as shown in Figure 32. It was designed to simulate heating the sample to normal operating temperatures, then rapidly heating the test specimen to induce thermal shock due to heat dump. Several tests were performed to various maximum temperature levels.

[3] D. Pantano and P. Joy, "Emergency Heat Rejection Test Results For Microtherm HT", Lockheed Martin Report PIR-U-SRG110-002A, (2/22/05).

Table 11. Heating Schedule Used for Heat Dump Testing

Lepel Power Setting (%)	Temperature Target (°C)	Heating Rate (°C/min.)
10-18	700	5
18	700	(30 minute hold)
50-75	1325	≈135

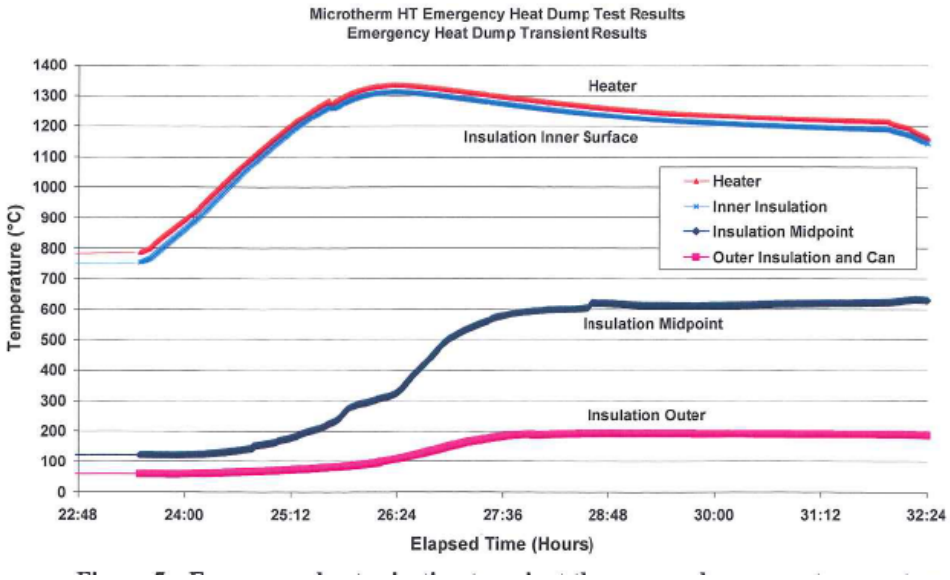

Figure 32. Emergency heat rejection thermocouple average temperature measurements from Lockheed Martin testing.

After testing, analysis of the exposed specimen was performed first through visual examination, then through sectioning and mounting the sample for optical and SEM with energy dispersive spectroscopy (EDS). Finally, the sample was analyzed by X-ray diffraction. Photographs of samples before and after testing are shown in Figure 33**.** As can be seen visually, testing causes the samples to change from beige to grey in color. Additionally, extensive cracking of the sample is evident after testing and significant deformation of the sample has occurred. Only slight changes in sample dimensions in the cross section were evident visually, but the sample had visibly shrunk in height. Changes in dimensions were on the order of 1 mm in the cross section and 2-5 mm in the height. Optical microscopy of the cross section sample areas (Figure 34) showed significant damage to the microstructure due to testing. The sample before testing had a smooth even appearance with small areas of porosity. Following testing, cracking was found to be present throughout the sample connecting the areas of porosity.

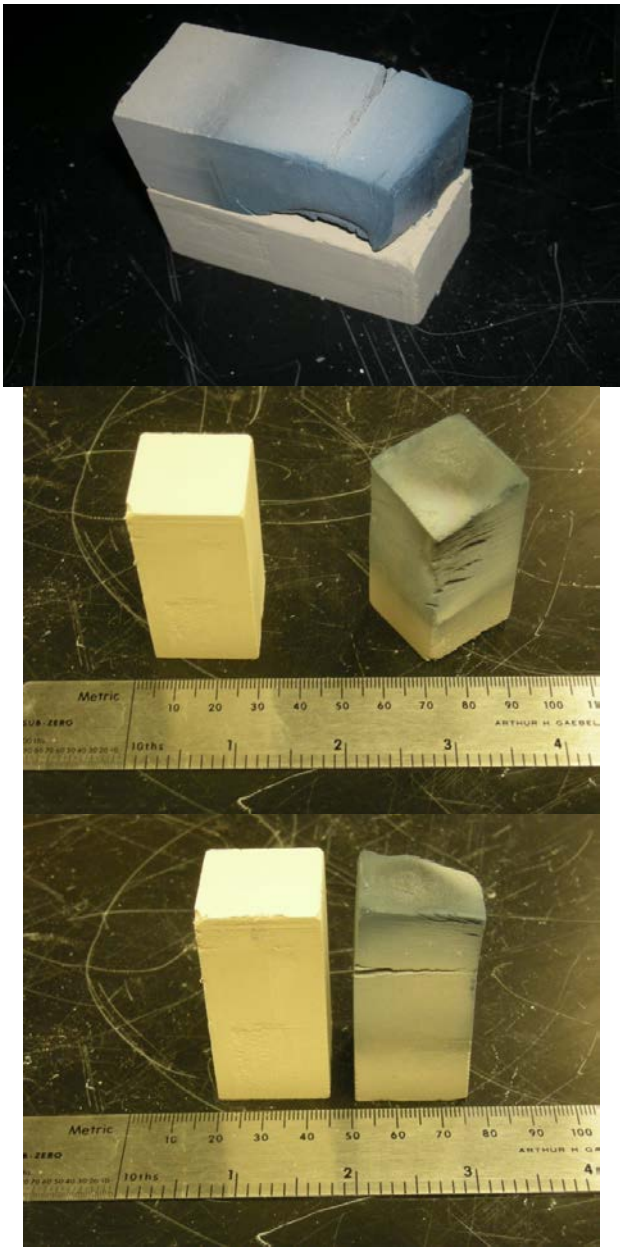

Figure 33. Comparison of Microtherm samples before and after testing.

(Note: Samples prior to testing have beige color; samples after testing have grey color)

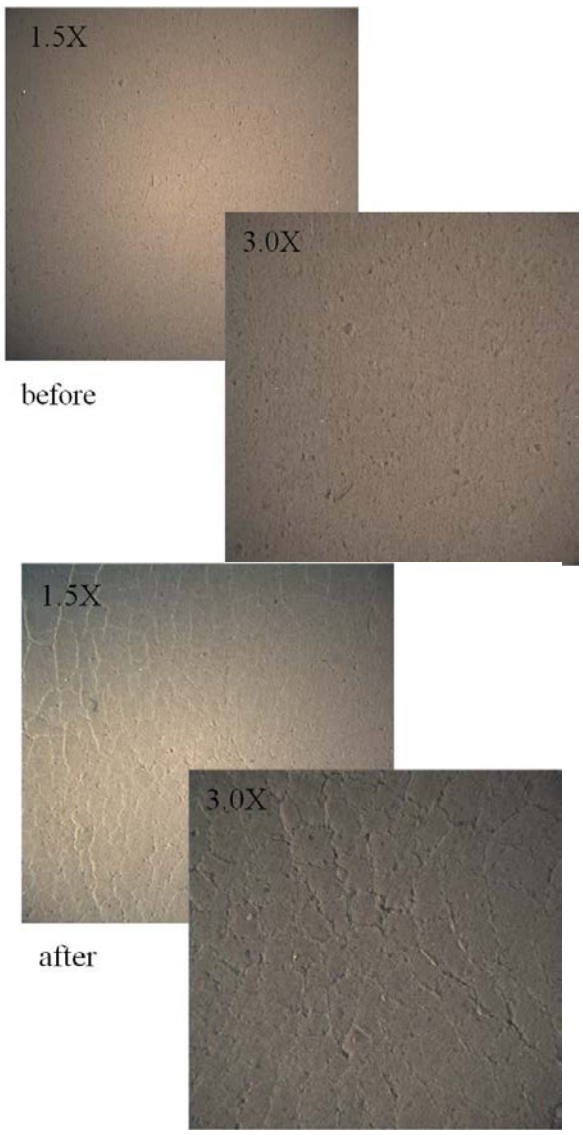

Figure 34. Optical microscopy of Microtherm samples before and after testing.

SEM/EDS analyses of the cross section sample areas before and after testing are shown in Figure 35. Again, before testing the cross section has an even appearance with light bands of material in a darker matrix. Only silicon and oxygen were found in the sample through the EDS analysis before testing (Figure 35(a)). Following testing, the sample was found to still contain silicon and oxygen, but significant amount of aluminum was also detected (Figure 35(b)). Note that carbon observed in both spectra is due to the coating on the SEM sample applied to prevent charging during analysis.

Standard powder X-ray diffraction was also performed on Microtherm samples before and after testing. The Microtherm sample analyzed prior to testing showed only titania (TiO_2) in two forms (anatase and rutile). It would be expected that silica and alumina would be present in this sample, but they were not observed. The samples analyzed after testing both still showed the presence of rutile, along with what was analyzed as the silicon carbide (SiC) compound (Moisonite). This identification is expected to be in error and what was actually seen was silica. If this is the case, then the silica content would be higher in the darker end of the sample then in the lighter end of the sample post testing. The sample taken from the bottom area post shock and the darker sample shows approximately half the rutile content as that shown by the lighter sample.

3.2.5 Key Results and Findings

1. Microtherm block material obtained from Lockheed was successfully machined into rectangular samples (25.4 x 25.4 x 50.8 mm) for testing through a procedure based on previous experience shared by Lockheed personnel.

2. A method was developed for observing the dimensional change of Microtherm during simulated isothermal high temperature “bake-out” through the utilization of a transparent furnace system produced by Thermcraft Incorporated (Winston Salem, NC) and high resolution video camera. Three tests were run with this system showing some general increase in sample size with heating followed by shrinkage of the sample with time at elevated temperature. Testing was completed for a maximum hold time of 190 hours at temperature and the maximum temperature of 850°C.

3. A Microtherm sample was thermally shocked at 930^{o}C using induction rapid heating techniques to simulate the actual temperature conditions experienced by the lining material during introduction of the fueled heater. Following testing the sample was analyzed visually revealing cracking or delamination of the sample approximately ¼ of the way from the top of the specimen due to heating.

4. Based on previous experience at ORNL, testing was carried out on Microtherm samples subjected to gradient temperature conditions under both vacuum and argon environments. Initially, six gradient tests were performed with an upper platen temperature of 850°C and a lower platen temperature of 250°C (three tests performed under vacuum environment and three tests performed under argon). A log equation ($y = a*\ln(x) + b$) was used to fit each shrinkage curve and an average curve was generated for general shrinkage under the vacuum and argon environments. SEM/EDS analysis was performed on Microtherm samples following testing showed cracking and fiber pull-out along with chemistry changes.

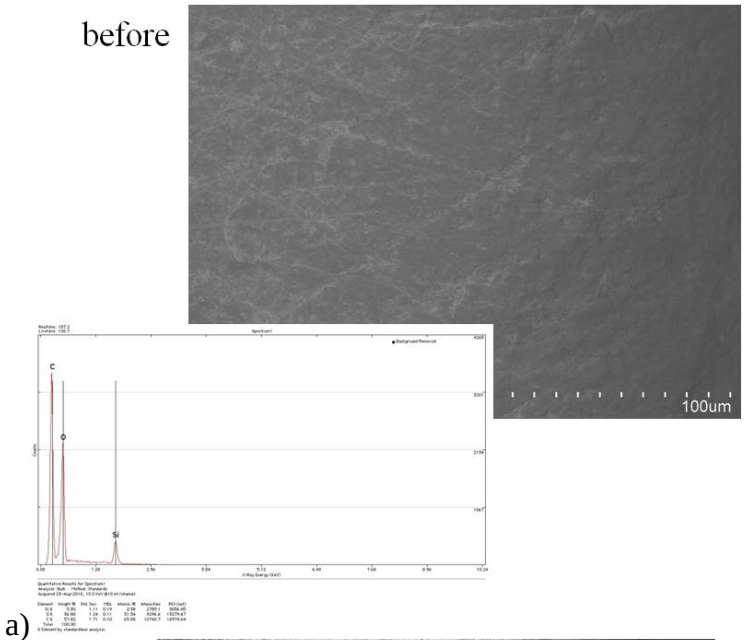

Figure 35. SEM/EDS analysis of Microtherm samples before (a) and after (b) testing.

Isothermal testing of Microtherm samples at various temperatures was conducted to generate shrinkage data that could be used to form a mathematical model to predict shrinkage over any gradient temperature condition of interest based on previous work at ORNL. Testing was conducted at 200, 400, 600, 700, and 800°C for various durations with the same log equation above fit to each shrinkage curve. The log curve fits for each temperature where then used to form a comprehensive model to estimate Microtherm shrinkage over any temperature gradient. It was found that the total predicted shrinkage using this model fit well with actual average measured shrinkage previously experimentally measured using the equation:

$$y = a*\ln(t)-b \quad (1)$$

where: $a = -8.786E\text{-}9*x^2 + 2.648E\text{-}6*x - 5.335E\text{-}4$

t = time in hours

$b = -8.738E\text{-}9*x^2 + 5.700E\text{-}6*x - 1.695E\text{-}3$

x = temperature in °C of sample location

Based on the success of this prediction, a follow-on gradient test was run under vacuum with a temperature gradient of 600-200°C. A similar analysis was run using the log curve fit model developed above. Again, it was found that the total predicted Microtherm shrinkage over this gradient fit well with the actual average measured shrinkage from experimental testing.

5. Testing to simulate ASRG engine failure conditions (termed as “heat dump” condition) were performed. Microtherm samples were rapidly heated using an induction rapid heating system to simulate the actual heating experienced by the lining material followed by a “simulated heat dump” event. Tests were completed at maximum temperatures of 1240 and 1325°C. Following testing, visual analysis of samples, optical microscopy, SEM/EDS, and X-ray diffraction revealed changes in sample appearance, size, microstructure, and chemistry.

INTERNAL DISTRIBUTION

1. B. R. Friske
2. E. P. George
3. J. G. Hemrick
4. J. M. Holladay
5. J. F. King
6. R. G. Miller
7. E. K. Ohriner
8. G. R. Romanoski
9. G. B. Ulrich
10. K. R. Veach, Jr.
11. ORNL Laboratory Records—OSTI

EXTERNAL DISTRIBUTION

12-16. U. S. DEPARTMENT OF ENERGY, NE-75/Germantown Building, 1000 Independence Avenue S. W., Washington, DC 20585-1290

R. Bechtel
W. A. Bohne
D. Cairns-Gallimore
A. K. Caponiti
W. S. Yoon

17. DEPARTMENT OF ENERGY, Oak Ridge Site Office, Building 4500N, Oak Ridge, TN 37831

S. R. Martin, Jr., Mail Stop 6269

18-19. IDAHO NATIONAL LABORATORY, P. O. Box 1625, Idaho Falls, ID 83415

K. L. Lively
S. G. Johnson

20. LOS ALAMOS NATIONAL LABORATORY, MS E525, Los Alamos, NM 87545

D. L. Armstrong

21-22. ORBITAL SCIENCES CORPORATION, INC., 20030 Century Blvd., Suite 102, Germantown, MD 20874

R. T. Carpenter
E. A. Skrabek

23. URS Safety Management Solutions, 2131 South Centennial Ave., Aiken, SC 29803

J. Barber